STUDY OF INTERFACIAL PHENOMENA IN THIN FILMS USING PHOTOELECTRON SPECTROSCOPY

by

Anoop Mathew

A thesis submitted to the Faculty of the University of Delaware in partial fulfillment of the requirements for the degree of Master of Science in Materials Science and Engineering

Spring 2006

© 2006 Anoop Mathew
All Rights Reserved

UMI Number: 1435840

UMI Microform 1435840

Copyright 2006 by ProQuest Information and Learning Company.
All rights reserved. This microform edition is protected against
unauthorized copying under Title 17, United States Code.

ProQuest Information and Learning Company
300 North Zeeb Road
P.O. Box 1346
Ann Arbor, MI 48106-1346

STUDY OF INTERFACIAL PHENOMENA IN THIN FILMS USING PHOTOELECTRON SPECTROSCOPY

by

Anoop Mathew

Approved: ____

Robert L. Opila, Ph.D.
Professor in charge of thesis on behalf of the Advisory Committee

Approved: ____

John F. Rabolt, Ph.D.
Chair of the Department of Materials Science and Engineering

Approved: ____

Eric W. Kaler, Ph.D.
Dean of the College of Engineering

Approved: ____

Conrado M. Gempesaw II, Ph.D.
Vice Provost for Academic and International Programs

ACKNOWLEDGEMENTS

I wish to thank my adviser, Dr. Robert Opila; and my friends and colleagues, especially Korhan Demirkan, Conan Weiland, Moses Haimbodi and other members of the Opila Group.

I would also like to acknowledge help from our collaborators at ASM America Inc., Chang-Gong Wang, Steven Marcus and Glen D. Wilk, collaborators from Rutgers, L. Goncharova and T. Gustafsson, and all the beamline personnel and support staff at the U4A beamline at Brookhaven National Laboratories. I would also like to thank Lijie Bao of Dupont Inc. and Les Fleming of North Carolina State University for the Lanthanum Aluminate and Titanium Silicate samples, the John Xiao group at the University of Delaware especially Weigang Wang and Grace Sheng for Magnetic Tunnel Junction samples, and Laura Parrish and Brian Willis for the Copper Oxide Samples. I also thank my family whose support has made all this possible.

TABLE OF CONTENTS

LIST OF FIGURES . . . . **vi**
LIST OF TABLES . . . . **ix**
ABSTRACT . . . . **x**

Chapter

1 INTRODUCTION **1**

1.1 X-ray Photoelectron spectroscopy 1
1.2 High-κ dielectrics 2

1.2.1 Film Preparation 5

1.3 Band alignment study of the interface between an oxide and TiN 5
1.4 Thin films for Magnetic Tunnel Junction (MTJ) Systems 6
1.5 Oxidized copper thin films for thin film interconnect applications 6

2 COMPOSITION AND LOCAL BONDING STRUCTURE **7**

2.1 Compositional information 7
2.2 Local bonding structure 8

3 TRENDS IN BINDING ENERGY AS A FUNCTION OF COMPOSITION **10**

3.1 Photoemission Data 10

4 PHASE STABILITY STUDIES **18**

4.1 Hafnium Nitride 23

5 MAXIMUM ENTROPY BASED DEPTH RECONSTRUCTIONS 27

5.1 Angle resolved photoemission 27
5.2 Maximum Entropy Algorithm 27
5.3 Comparison of Maximum Entropy with MEIS Data 32

6 VALENCE BAND SPECTROSCOPY STUDIES OF TIN/TA_2O_5 TIN/AL_2O_3 INTERFACES 36

6.1 Synchrotron Radiation 36
6.2 Beamline Characteristics 36
6.3 Experimental 37
6.4 Band Alignment 39
6.5 Future Experiments — Metal Gates for transistors 41

7 PHOTOEMISSION STUDY OF MAGNETIC TUNNEL JUNCTION INTERFACES 43

7.1 Magnetic Tunnel Junctions 43
7.2 Sample Preparation 45
7.3 Auger depth profile 46
7.4 XPS Results 46

8 PHOTOEMISSION EXPERIMENTS COMPLEMENTING THE STUDY OF COPPER ION TRANSPORT IN SIO_2 DIELECTRICS 50

8.1 Introduction 50
8.2 Experiment 51
8.3 Results & Discussion 53
8.4 Conclusions 55

9 FUTURE WORK 57

9.1 Interfacial Charge 57

BIBLIOGRAPHY 59

LIST OF FIGURES

1.1 Schematic of the X-ray photoemission setup 2

1.2 Cross section of a transistor showing the substitution of the SiO_2 dielectric with a new generation high-κ dielectric. (Source: Intel Inc)[1] 3

1.3 Schematic showing the layout of a CMOS transistor 4

2.1 Compositional information - three samples with progressively higher nitridation temperatures show progressively more intense N 1*s* photoelectron spectra. 8

2.2 Nitrogen 1*s* peak of a Hf Rich sample and a Silicon rich sample deconvolved into bonding states associates with Silicon and Hafnium . . 9

3.1 Illustration of how changing the second nearest neighbor atoms leads to changes in electron density of the atom being probed leading to changes in binding energy 11

3.2 Shifts in the Binding energies of Hf 4*f*, Si^{4+} 2*p* and O 1*s* for unannealed thin films as a function of composition 12

3.3 Hf 4*f* as a function of composition of the non-nitrided hafnium silicates. 13

3.4 Shifts in the Binding energies of La 3*d*, Al 2*p* and O 1*s* for unannealed films as a function of composition 14

3.5 Shifts in the Binding energies of Ti 2*p*, Si 2*p* and O 1*s* for unannealed films as a function of composition 15

3.6 Photoemission Spectra for unnannealed films showing Ti 2*p*, Si 2*p* and O 1*s* as a function of composition 16

4.1 Hf 4*f* Binding energy for non-nitrided and nitrided hafnium silicates before and after rapid thermal annealing to 950°C for 10s. The intensities have been normalized for comparison purposes. 20

4.2 Si 2*p* Binding energy for non-nitrided and nitrided hafnium silicates before and after rapid thermal annealing to 950°C for 10s. The Si^0 2*p* intensities have been normalized for comparison purposes. 21

4.3 Hf 4*f* and Si 2*p* as a function of various processing conditions 22

4.4 Hf 4*f* for a HfN sample prepared using ALD curvefit to three components, shown before and after anneal in vacuum to 600°C for 1 hour. 23

4.5 O 1*s* and C 1*s* for a HfN sample prepared using ALD shown before and after Ar^+ sputter followed by an anneal in vacuum to 600°C for 1 hour. . 25

4.6 Hf 4*f*, N 1*s* for a HfN sample prepared using ALD shown before and after Ar^+ sputter followed by an anneal in vacuum to 600°C for 1 hour. . 26

5.1 Angle resolved photoemission – illustration of how the sampled depth changes with angle 28

5.2 Flow Chart outlining the program flow for depth profiling of the hafnium silicate using a maximum entropy algorithm 30

5.3 Evolution of the depth profiles for a hafnium silicate sample from the initial assumed profile (top) to the finally converged profile (bottom) . . 31

5.4 The metric 2[O] + 3[N] plotted for reconstructions obtained at three different temperatures is seen to remain roughly constant, suggesting consistent results. 33

5.5 Trends in oxygen versus nitrogen profiles for three hafnium silicate films nitrided at different temperatures as reconstructed by the maximum entropy method. The oxygen appears to be substituted by nitrogen at progressively higher temperatures. 34

5.6 Comparison of MEIS data and maximum entropy generated depth profile data. 35

6.1 Au and TiN Fermi Edges 37

6.2 Au and TiN secondary electron cutoffs 38

6.3 ALD Al_2O_3 and TiN Fermi Edges 39

6.4 PEALD Al_2O_3 and TiN Fermi Edges 40

6.5 Ta_2O_5 and TiN Fermi Edges 40

6.6 Band Alignment 41

7.1 MTJ Schematic 44

7.2 MTJ Underoxidized vs Overoxidized illustrating how the degree of oxidation of the aluminum barrier can be expected to affect the properties of the system. 45

7.3 MTJ Layer Scheme for a FeNi/Al_2O_3/FeNi setup 46

7.4 Auger Depth profile for a FeNi/Al_2O_3/FeNi MTJ sample validating the compositional depth profile of the film. 47

7.5 Depth Profile showing Al_2O_3 in a Co(160Å) / Al-oxide(10Å) / Co (85Å) / FeMn (85Å) /Cu (72Å) /FeNi (215Å) / Si structure. 48

7.6 Photoemission peak of the oxidized Al_2O_3 peak showing its peak energy at a binding energy higher than 74.4eV, expected for Al_2O_3. 48

8.1 Compositional Depth Profile showing variation of Copper, Oxygen and Silicon concentration with depth: (a, b) – thermal oxidation of Cu films; (c) – prepared by reactive sputtering 52

8.2 Copper 2 *p* Depth Profile: (a, b) – thermal oxidation of Cu films; (c) – prepared by reactive sputtering 54

8.3 Oxygen 1*s* Depth Profile: (a, b) – thermal oxidation of Cu films; (c) – prepared by reactive sputtering 56

9.1 Presence of interfacial charges in the system affect the binding energies of the emitted photoelectrons. 58

LIST OF TABLES

3.1 Slopes of various elemental binding energies as a function of composition in three different material systems – $LaAlO_3$, $HfSiO_4$ & $TiSiO_4$ 13

4.1 Atomic concentrations of the various elements in HfN varying with treatment. 23

ABSTRACT

The study of thin films and their interfaces is an important area of research in modern microelectronics. This study looks at four such interfaces using X-Ray photoelectron spectroscopy. The first of these involves high-κ dielectrics for replacing the silicon dioxide gate dielectric in the conventional CMOS transistor for reduction of gate leakage currents. A maximum entropy based algorithm is used to non-destructively reconstruct compositional depth profiles from angle resolved photoemission data. Considered next is the band alignment of the interface between oxides and titanium nitride, useful for understanding leakage currents in Metal-Insulator-Metal (MIM) capacitors. Another system studied is the oxide / ferromagnet interface in a magnetic tunnel junction (MTJ) — photoemission provides insights here about what affects the performance of devices like magnetic memory (MRAM) for which it can be used. The last system that is investigated involves the study of copper diffusion in silicon dioxide for interconnect applications.

Chapter 1

INTRODUCTION

Thin films and their interfaces are important areas of study for many critical technologies. This study looks at four example of thin films and their interfaces. The primary tool of investigation has been X-ray photoemission spectroscopy (XPS). This study focuses on:

- Insulating films for High-κ dielectric applications
- Band alignment of the interface between Ta_2O_5 and TiN
- Thin films for Magnetic Tunnel Junction (MTJ) Systems
- Oxidized copper thin films for thin film interconnect applications

1.1 X-ray Photoelectron spectroscopy

X-ray Photoelectron spectroscopy (XPS) is a good tool for investigating these thin dielectric films. In XPS, the sample is irradiated with monochromated X-ray radiation, (typically the Al K_α at 1486.6 eV in our experimental setup — using a PHI 5600 XPS), and this excites photoelectrons from the core levels of the sample. Since the electron attenuation length is typically of the order of 2 to 3 nm, the effective sampling depth achieved by photoemission is ideal for studying these thin films 4 to 5 nm thick.

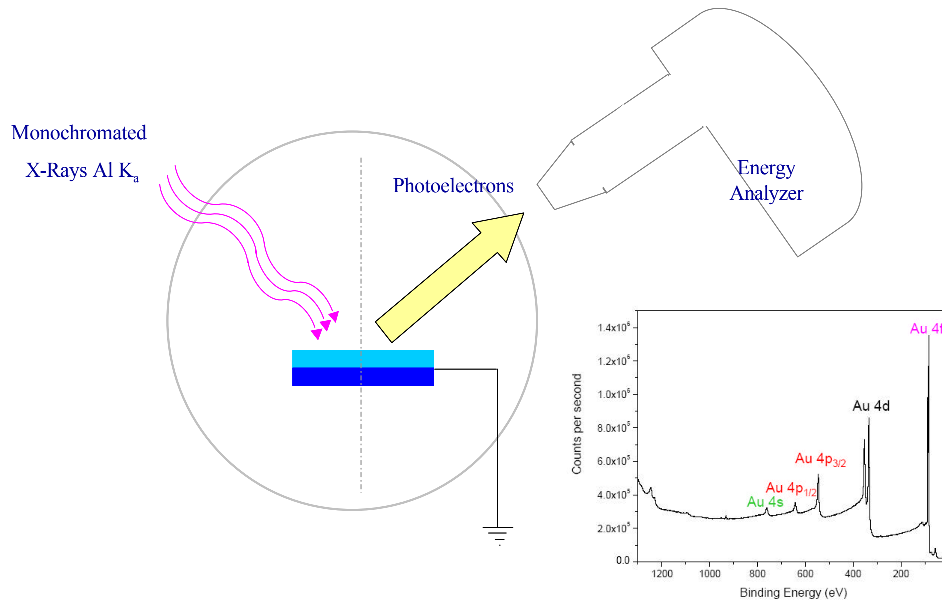

Figure 1.1: Schematic of the X-ray photoemission setup

1.2 High-κ dielectrics

Continuous improvements in integrated circuit performance are possible today because of the semiconductor industry's ability to scale device dimensions allowing greater density of transistors on a chip, resulting in higher speeds and reduced costs. Device scaling has so far followed Moore's Law[2] which predicts the doubling of the number of transistors on integrated circuits roughly every 18 months. With the scaling of feature sizes, leakage current that results from tunneling through the gate oxide in the CMOS transistor is a problem. High-κ dielectrics are a class of materials that are being investigated today for proposed changes to the gate dielectric. The transition from using the conventional gate dielectric, SiO_2 to materials that decrease the gate leakage current raises a variety of challenges in integration with the rest of the chip. Key considerations that guide the choice of the dielectric include its dielectric constant, band gap, band alignment to silicon, thermodynamic stability, film morphology, interface quality, compatibility with the

CMOS device materials, process compatibility, and reliability[3]. Channel mobilities of electrons and holes need to be maintained at approximately 90% of their values in SiO_2 devices. Device performance and reliability metrics need to be essentially the same as SiO_2, which implies that the interfacial and bulk defect densities such as interfacial traps, D_{it}, and fixed charge, Q_f, must be less than 10^{11} cm^{-2} and defect generation under accelerated stress bias testing must correspond to times to failure of about 10 years[4]. The stability of the dielectrics to chemical phase separation under temperatures for processing these materials such as dopant activation in the source and drain contacts at temperatures approaching 1000°C is also critical. Replacing the polysilicon metal electrode with alternative metal gates is also being actively considered in view of issues such as insufficient number of charge carriers during transistor channel inversion.

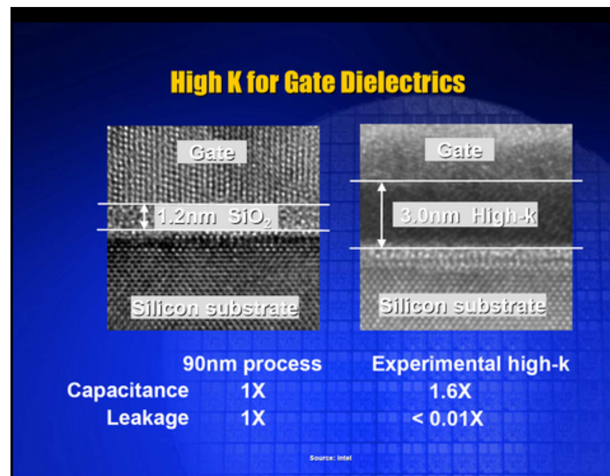

Figure 1.2: Cross section of a transistor showing the substitution of the SiO_2 dielectric with a new generation high-κ dielectric. (Source: Intel Inc)[1]

From a simple electrical standpoint, the metal-oxide-semiconductor structure is equivalent to a parallel plate capacitor. Consider the capacitance, C, where A is the capacitor area, κ is the relative dielectric constant of the material (3.9 for SiO_2), ϵ_0 is the

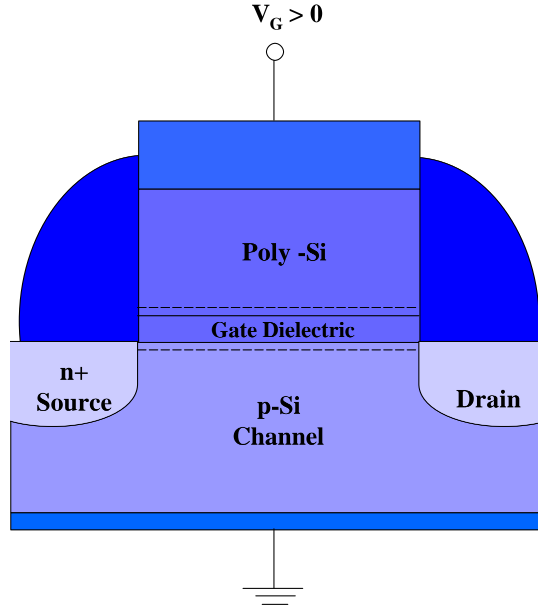

Figure 1.3: Schematic showing the layout of a CMOS transistor

permittivity of free space and t_{ox} is the gate oxide thickness. As the density of circuit elements increase, the area decreases. If we consider capacitance to be a figure of merit we need to preserve, we need to decrease the thickness t_{ox} or increase the dielectric constant, κ. Since the reduction in the thickness t_{ox} has reached a point where further reductions would result in unacceptably high leakage currents, increasing κ is one way to continue device scaling, hence the need for high-κ dielectrics.

An often used metric is the equivalent oxide thickness (EOT, t_{eq}), which represents the theoretical thickness of SiO_2 that would be required to achieve the same capacitance density as the dielectric, ignoring issues such as leakage current and reliability.

$$\frac{t_{eq}}{\epsilon_{r,SiO_2}} = \frac{t_{high-\kappa}}{\epsilon_{r,high-\kappa}} \tag{1.1}$$

Ultimately, we can use much thicker layers of the alternative dielectric, for example a 51Å thick layer of HfO_2 ($\kappa = 20$) to achieve the capacitance equivalent to a 10Å thick SiO_2 layer - the equivalent oxide thickness of the HfO_2 layer is thus 10Å.

Hafnium silicates are the most likely candidates for implementation of the high-κ dielectrics at the 65 nm technology node. They are nitrided to prevent boron diffusion from the heavily doped polysilicon to the channel. The determination of the nitrogen profile in these films is very important and a non-destructive technique could be a very useful probe. A maximum entropy based depth profile reconstruction from angle resolved photoemission is thus expected to fill this niche in this regard.

1.2.1 Film Preparation

Atomic Layer Deposition (ALD) is a chemical gas phase method involving sequential saturating, self limiting surface reactions. It involves alternate pulses of precursors separated by purge steps. ALD has several advantages such as atomic level control of film composition, accurate thickness control at the monolayer level, large, uniform area and batch capabilities, excellent conformality including that for sharp interfaces, good reproducibility, ability to use precursors with high mutual reactivity, and the ability to deposit high quality films at low deposition temperatures[5, 6, 7]. These advantages make ALD the chosen method for depositing these high-κ dielectrics.

For our study, $(HfO_2)_x(SiO_2)_{1-x}$ films were deposited using atomic layer deposition (ALD) at ASM America Inc. Some of the samples were then thermally nitrided at different temperatures. A variety of hafnium silicates with varying hafnia to silica ratios and different nitridation conditions were analyzed using photoemission.

1.3 Band alignment study of the interface between an oxide and TiN

The interface between titanium nitride (TiN) and Ta_2O_5 or Al_2O_3 is an interesting system studied for metal-insulator-metal (MIM) capacitor applications. Synchrotron radiation is a good source of ultraviolet photons that can be used for studying the valence band edge of titanium nitride and its interface with insulating oxides. This constitutes the second part of the study of thin film interfaces.

1.4 Thin films for Magnetic Tunnel Junction (MTJ) Systems

Magnetic Tunneling Junctions (MTJ's) constitute an important technology that is important to the development of magnetic random access (MRAM) memories and other spin electronic devices[8, 9, 10]. In this study, we characterize the FeNi/Al_2O_3/FeNi and Co/Al_2O_3/Co MTJ which poses several interesting questions such as the presence of charge accumulation at FeNi/Al_2O_3 or Co/Al_2O_3 interface and the interfacial chemistry associated with such systems. Photoemission can give us compositional, chemical, and electronic properties of this system, which can then be correlated to various other properties of this interface.

1.5 Oxidized copper thin films for thin film interconnect applications

Diffusion barrier layers are used to prevent the migration of copper into active device regions and the associated degradation of the dielectric properties of the insulator in course of the integration of copper interconnects with silicon based microelectronics[11, 12]. This part of the study complements investigations characterizing this interface[13, 14] by providing compositional information of these systems as a function of depth.

Chapter 2

COMPOSITION AND LOCAL BONDING STRUCTURE

2.1 Compositional information

The current study utilizes photoemission as a tool to study the compositional structure and nature of the local bonding in various hafnium silicates that are potential candidate materials for replacing the silicon dioxide dielectric at the 65 nm technology node for low standby power applications. Depending on the number and combination of other atoms attached to the nitrogen atom, the photoemission peak is expected to vary in energy because of different electronegativities of the atoms and the resulting change in ease of photoexcitation of these atoms. A simplified view of this process can approximate the expected components in the N 1*s* peak to be reduced to one involving the nitrogen atom bonded to only hafnium atoms, and another involving the nitrogen bonded to only silicon atoms. Deconvolving the nitrided hafnium silicate peak energies is expected to reflect the nature of the varied bonding states in the system, similar to the bonding states observed by Chang *et al.*[15] in a silicon oxynitrides film.

Figure 2.1 shows the utility of photoemission studies in elucidating compositional information. Three hafnium silicate films deposited using atomic layer deposition are compared here. The three films were thermally nitrided using ammonia at three different temperatures, 700°C, 800°C and 900°C. The area under the photoemission peak is proportional to the amount of the element present. With the appropriate sensitivity factor, we can extract the compositional information from the films of interest. As expected, the samples processed at higher nitridation temperatures exhibited higher nitrogen concentrations. There is a slight component at a higher binding energy corresponding to

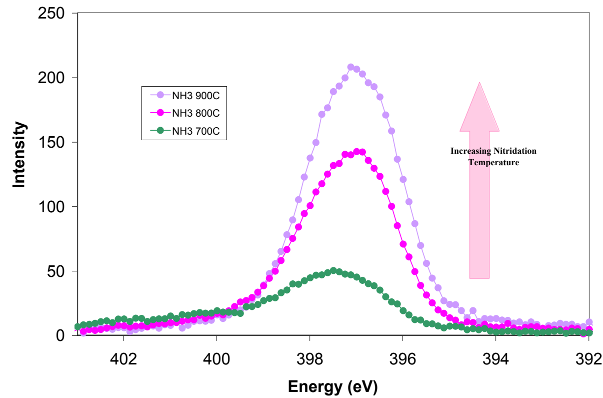

Figure 2.1: Compositional information - three samples with progressively higher nitridation temperatures show progressively more intense N 1*s* photoelectron spectra.

the bonding state associated with the nitrogen atoms bonded to oxygen atoms of higher electronegativity.

2.2 Local bonding structure

Figure 2.2 shows the nitrogen peak deconvolved into two components, one representative of the nitrogen bonded to the silicon and the other corresponding to the nitrogen bonded to the hafnium atoms. Since the silicon atom has the higher electronegativity (electronegativity of Si=1.9, compared to electronegativity of Hf=1.3), or greater electron withdrawing power, the component corresponding to the N-Si bond appears at the higher binding energy since the electron is now harder to extract using photoemission. For fitting the N 1*s* peak, in order to obtain a constrained fit, the value of the N-Si_3 bond taken to be 397.5 and FWHM 1.5 eV from Chang *et al.*[15]

For the silicon rich sample, the ratio of atomic concentrations of Si:Hf = 1.72:1.

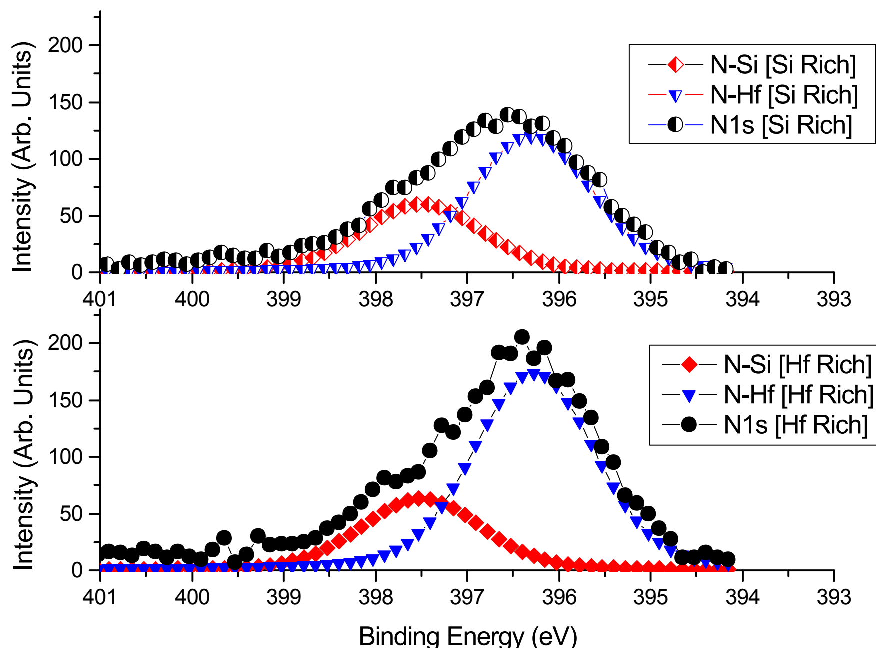

Figure 2.2: Nitrogen 1*s* peak of a Hf Rich sample and a Silicon rich sample deconvolved into bonding states associates with Silicon and Hafnium

The ratio of N-Si:N-Hf = 0.502:1. The ratio between these two ratios = 0.29. For the relatively Hf rich sample, the ratio of atomic concentrations of Si:Hf = 1.26:1. The ratio of N-Si:N-Hf = 0.36:1. The ratio between these two ratios = 0.29. This can potentially be interpreted as a measure of the efficiency of nitrogen incorporation.

Comparing the two plots, we conclude that the nitrogen preferentially bonds to hafnium atoms, as evidenced by the larger area under the N 1*s* peak for the hafnium rich silicate as well as the relatively larger proportion attributed to the N-Hf component for the hafnium rich sample.

Chapter 3

TRENDS IN BINDING ENERGY AS A FUNCTION OF COMPOSITION

Reports in literature have documented trends in binding energy of the metal and silicon photoemission peaks as a function of metal composition[16] due to second nearest neighbor interactions. We investigated these trends as a function of composition of these materials, and processing conditions such as nitridation and annealing. We investigated this behavior in three different material systems — $(HfO_2)_x(SiO_2)_{1-x}$, $(La_2O_3)_x(Al_2O_3)_{1-x}$ and $(TiO_2)_x(SiO_2)_{1-x}$.

The hafnium silicate samples were synthesized using Atomic Layer Deposition by our collaborators Wang and Wilk *et al.*[17, 18, 19] at ASM America Inc. Lanthanum aluminates were deposited by sputter deposition by Lijie Bao of Dupont Inc. The titanium silicates we studied were deposited using remote plasma deposition by our collaborators Fleming and Lucovsky *et al.* [20, 21, 22, 23, 24] from North Carolina State University.

3.1 Photoemission Data

Data on the Hf 4*f*, Si 2*p* and O 1*s* binding energies (Fig. 3.2) confirm shifts in binding energies as a function of composition. Opila *et al.*[16] have reported that this behavior is attributable to the second nearest neighbor effect. This is illustrated in figure 3.1. As expected, increasing the Hf^{4+} ion content decreases the binding energy of all the peaks since it is a lower electronegativity element effectively replacing the more electronegative Si^{4+} atoms as the second nearest neighboring atoms, thus making the

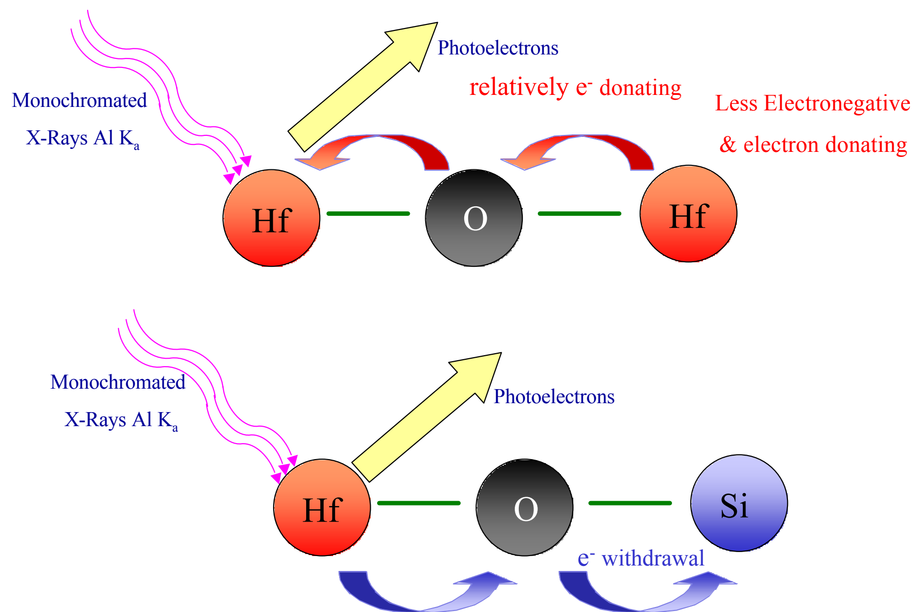

Figure 3.1: Illustration of how changing the second nearest neighbor atoms leads to changes in electron density of the atom being probed leading to changes in binding energy

photoemission of electrons bound to the interrogated atom easier. Yu *et al.*[25, 26] have reported observing similar behavior in hafnium aluminates. Further studies are planned including investigation of the presence or absence of such shifts when the samples are annealed or nitrided. Similar trends in the binding energies of N 1*s* would be interesting in the case of nitrided samples.

Table 3.1 tabulates the slopes of lines obtained from plotting a linear fit to the binding energy versus composition plot for the $(La_2O_3)_x(Al_2O_3)_{1-x}$, $(HfO_2)_x(SiO_2)_{1-x}$ and $(TiO_2)_x(SiO_2)_{1-x}$ systems. In an ideal system without interfacial charges, one might expect a good correlation between the difference in electronegativity of the two metal atoms involved and the slopes of their binding energy versus composition curve. This is not the case here, and slopes of the metallic peaks do not show good correlation with the

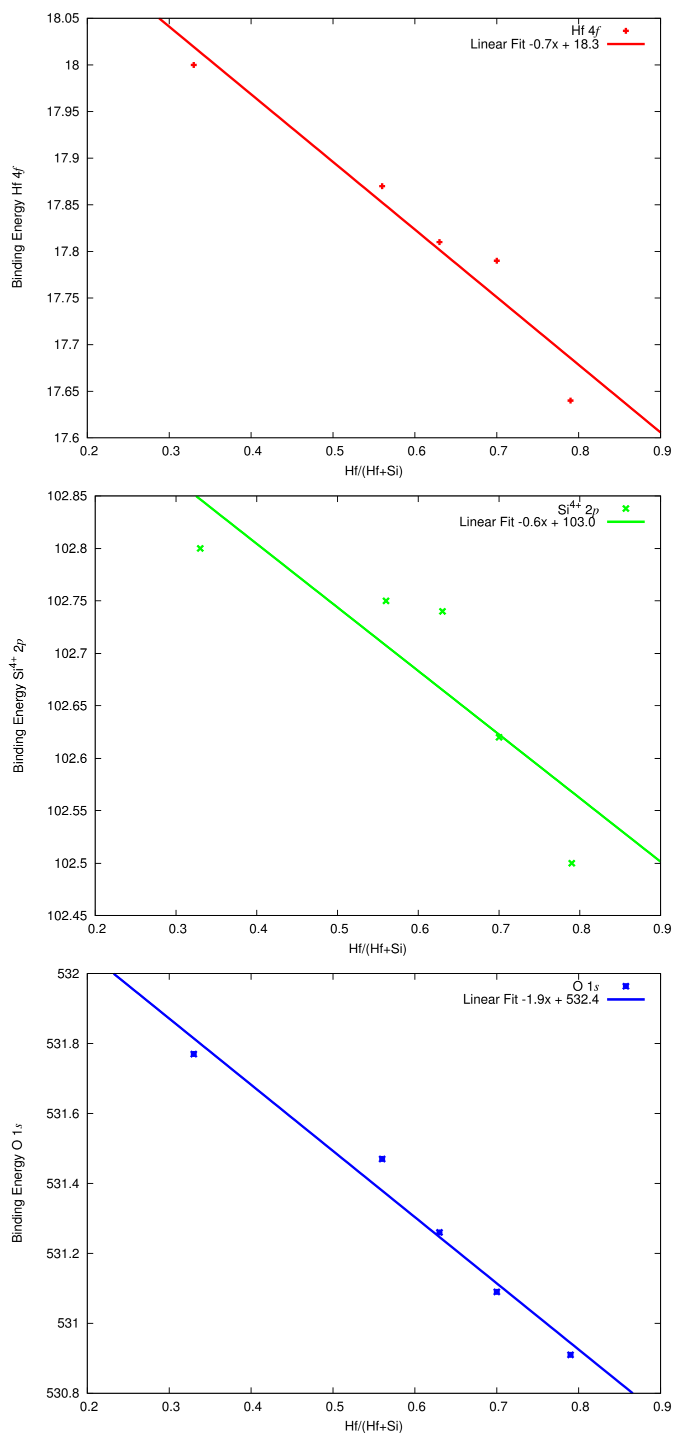

Figure 3.2: Shifts in the Binding energies of Hf 4*f*, Si^{4+} 2*p* and O 1*s* for unannealed thin films as a function of composition

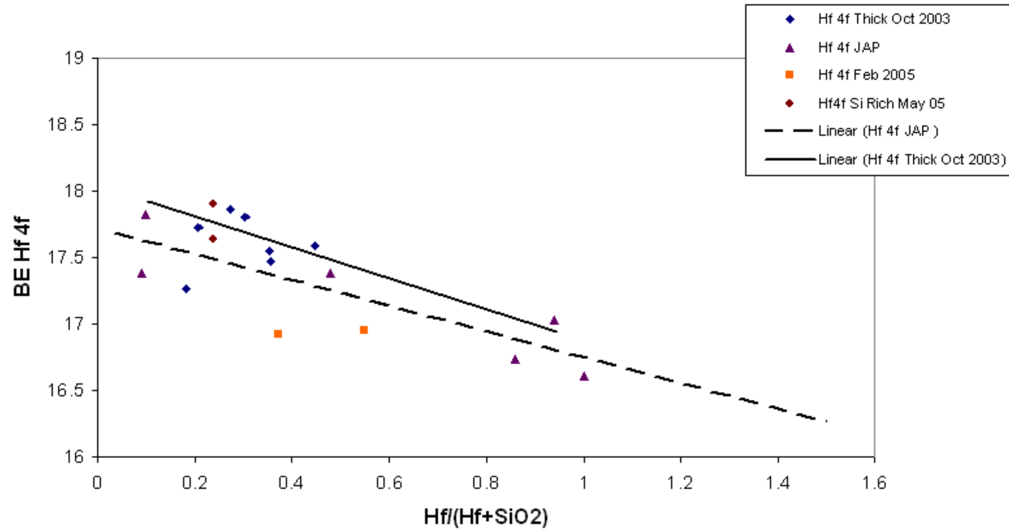

Figure 3.3: Hf 4*f* as a function of composition of the non-nitrided hafnium silicates.

Element	Electronegativity (Pauling)	Slope in $LaAlO_3$	Slope in $HfSiO_4$	Slope in $TiSiO_4$
La	1.1	-1.9 ± 0.04		
Hf	1.3		-0.7 ± 0.1	
Ti	1.54			-0.7 ± 0.1
Al	1.61	-1.8 ± 0.08		
Si	1.9		-0.6 ± 0.2	-1.4 ± 0.2
O	3.44	-2.2 ± 0.1	-1.9 ± 0.2	-2.9 ± 0.3

Table 3.1: Slopes of various elemental binding energies as a function of composition in three different material systems – $LaAlO_3$, $HfSiO_4$ & $TiSiO_4$

differences in electronegativity of the metals. This is partly because of different preparation methods for the three different films. Within the same set of films, if we compare slopes of one metallic ions with other, such as in lanthanum aluminates, the slopes of the La and Al lines are about the same — about -1.8, or in the case of hafnium silicates, the slopes of the Hf and Si are about the same — about -0.6. Interestingly, in the titanium

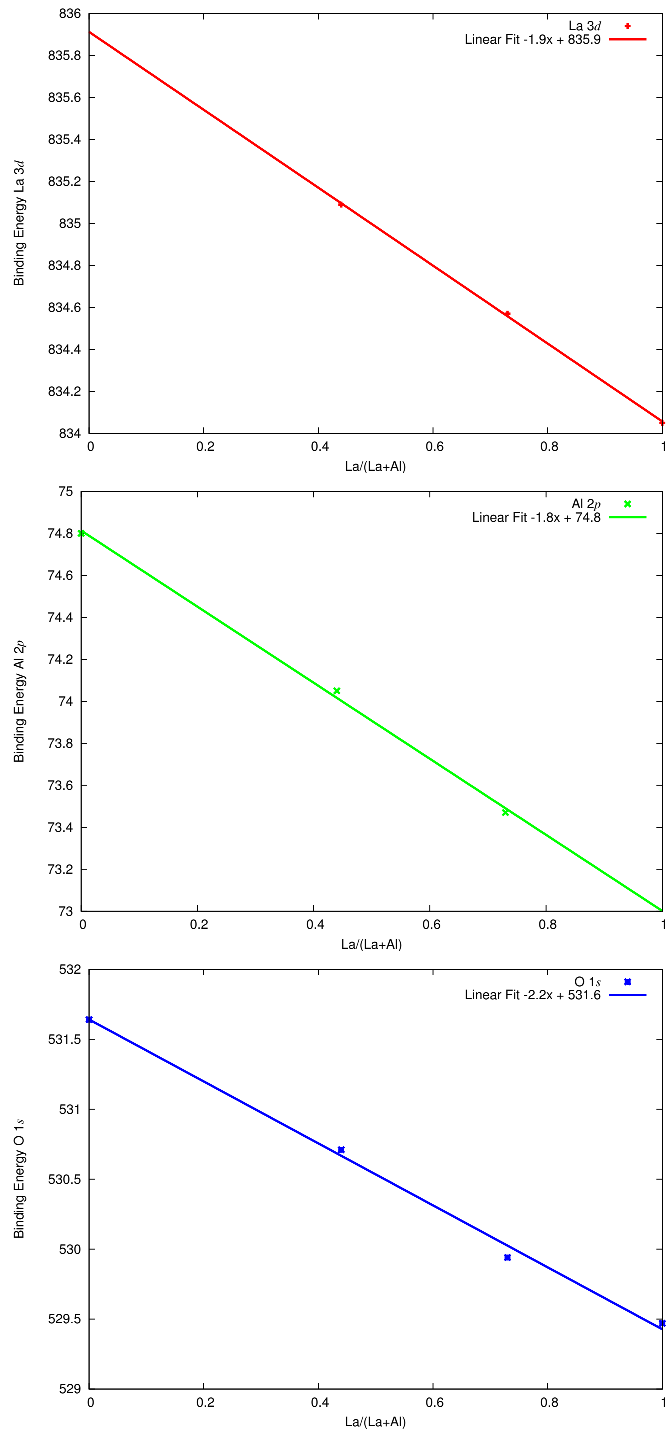

Figure 3.4: Shifts in the Binding energies of La 3*d*, Al 2*p* and O 1*s* for unannealed films as a function of composition

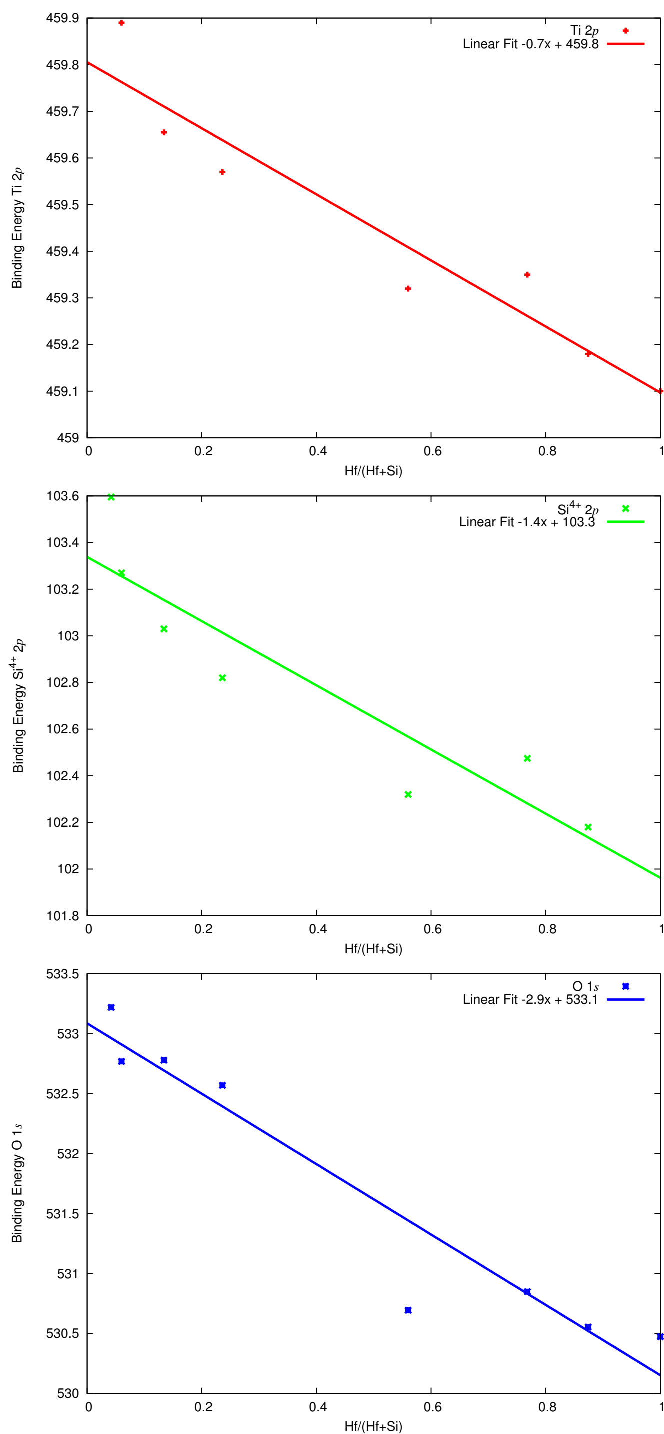

Figure 3.5: Shifts in the Binding energies of Ti 2p, Si 2p and O 1s for unannealed films as a function of composition

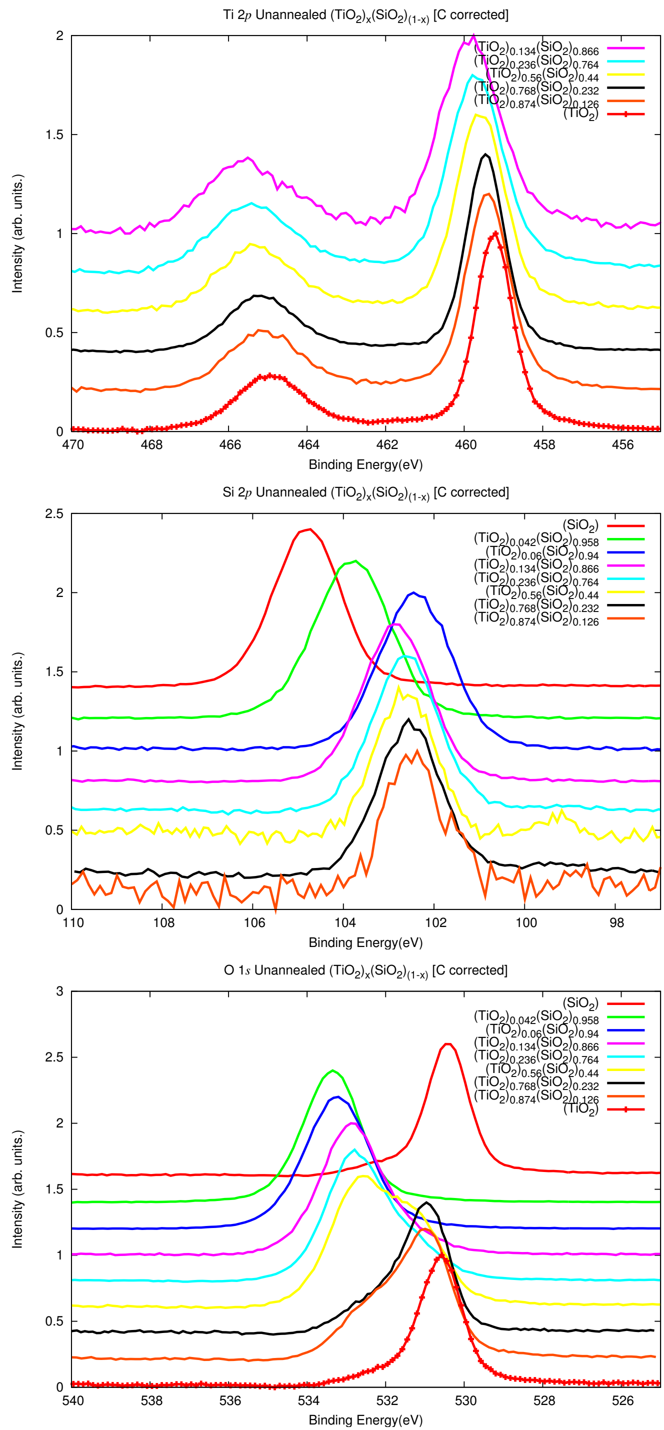

Figure 3.6: Photoemission Spectra for unnannealed films showing Ti 2p, Si 2p and O 1s as a function of composition

silicate, the slopes of the Ti and Si peaks are widely different, -0.7 for Ti as opposed to -1.4 for the Si peak. This could be interpreted as indicative of a network structure with a good deal of segregation in it, with a Si network that is not completely enmeshed with the Ti network, and with inbuilt charge layers. This could again be attributed to different preparation schemes of the materials.

In all cases, the slope of oxygen is a dominating number compared to the metal slopes (> 2.0). This is also understandable on the basis of the larger electronegativity of oxygen which makes the electron density on the oxygen atom more amenable for distortion, causing larger shifts in binding energy than for the metallic ions. This number could also be interpreted as indicative of the unique bonding geometries that the oxygen atoms involves itself in the network of mixed oxides. Figure 3.6 (c) showing the O 1*s* evolving with composition especially shows two pronounced humps in the photoemission peak which grow or get attenuated with changing composition. Further work, especially ab-initio calculations of electron densities of these species similar to ones done by Rignanese *et al.* [27, 28, 29] could give more hints on the nature of the change of these core level energies with varying stoichiometry of atoms with differing electronegativities.

Chapter 4

PHASE STABILITY STUDIES

An important requirement for the high-κ dielectric is the stability of the hafnium silicate in being able to withstand temperatures up to 1000°C for short times (typically 10-20 s), which is above the crystallization temperature of the metal oxide. Alloying the metal oxides with SiO_2 increases the crystallization temperature of the dielectric, though it reduces the dielectric constant[30]. Investigators have reported that hafnium silicate (as well as the zirconium silicate) films transform to a phase separated microstructure that consists of a crystalline HfO_2 or ZrO_2 rich phase embedded in an amorphous silica rich matrix[31, 32, 33]. Stemmer *et al.* have shown that the phase separation can be understood as a metastable phase equilibrium in which formation of the structurally complex crystalline silicate, requiring extensive atomic rearrangements, is kinetically excluded. This behavior, referred to as spinodal decomposition[34] is associated with the presence of a liquid miscibility gap in the $(HfO_2)_x(SiO_2)_{1-x}$ system. Monaghan *et al.*[35] have recently performed density functional calculations to study simulated thermal anneals and the resulting segregation mechanisms.

The rapid thermal annealing is expected to spinodally decompose amorphous films with compositions that lie within the metastable extensions of the spinodal inside the miscibility gap. Stemmer *et al.*[30] argue that during this demixing, the hafnia rich phase may exceed the crystallization temperature and crystalline HfO_2 will form. Rayner *et al.*[36] have conducted some spectroscopic investigations that track the phase separational behavior of zirconium silicates. Sayan *et al.*[37] have suggested the formation of a silicide in response to the thermal processing.

We used photoemission spectroscopy to study the position of the photoemission peaks of the resulting phases upon rapid thermal annealing of these films, investigating whether they correspond to positions of pure hafnia or silica or some energy state in between. The effect of nitrogen on such reported phase decomposition behavior will also be investigated. It would also be interesting to see if changes in processing conditions such as the use of plasma enhanced atomic layer deposition (PE ALD), thermal ALD or Metal Organic Chemical Vapor Deposition (MOCVD) deposition methods affect the phase stability.

Figures 4.1 and 4.2 show some preliminary data on the Hf 4*f* and Si 2*p* photoemission peak of a hafnium-rich and a silicon-rich sample, one set thermally nitrided with ammonia, and one not. The rapid thermal annealing was done at 950°C for 10s using an AG Associates Heatpulse 610. The spectra were referenced to the adventitious C 1*s* peak energy at 285.0 eV to correct for any differential charging effects. The Hf 4*f* peak in both the nitrided and non-nitrided samples shift to a higher binding energy upon annealing, away from the energy of the expected HfO_2 species, which is not keeping with expected behavior if one were to expect the material to phase segregate into HfO_2 and SiO_2 regions[38]. We will investigate reasons for this seemingly anomalous behavior. The Si^{4+} 2*p* peak energies of the annealed samples move closer to the SiO_2 peak position, which would be consistent with the idea of the sample phase segregating into hafnia and silica rich regions. The shifts in the Si^0 metallic peaks could be reflective of the presence of interfacial charges. Figure 4.3 summarizes the peak positions of both the nitrided as well as the non-nitrided sample before and after RTA in two plots. As summarized in the previous section, further work needs to be done to reconcile the observed photoemission we and others[39] have observed.

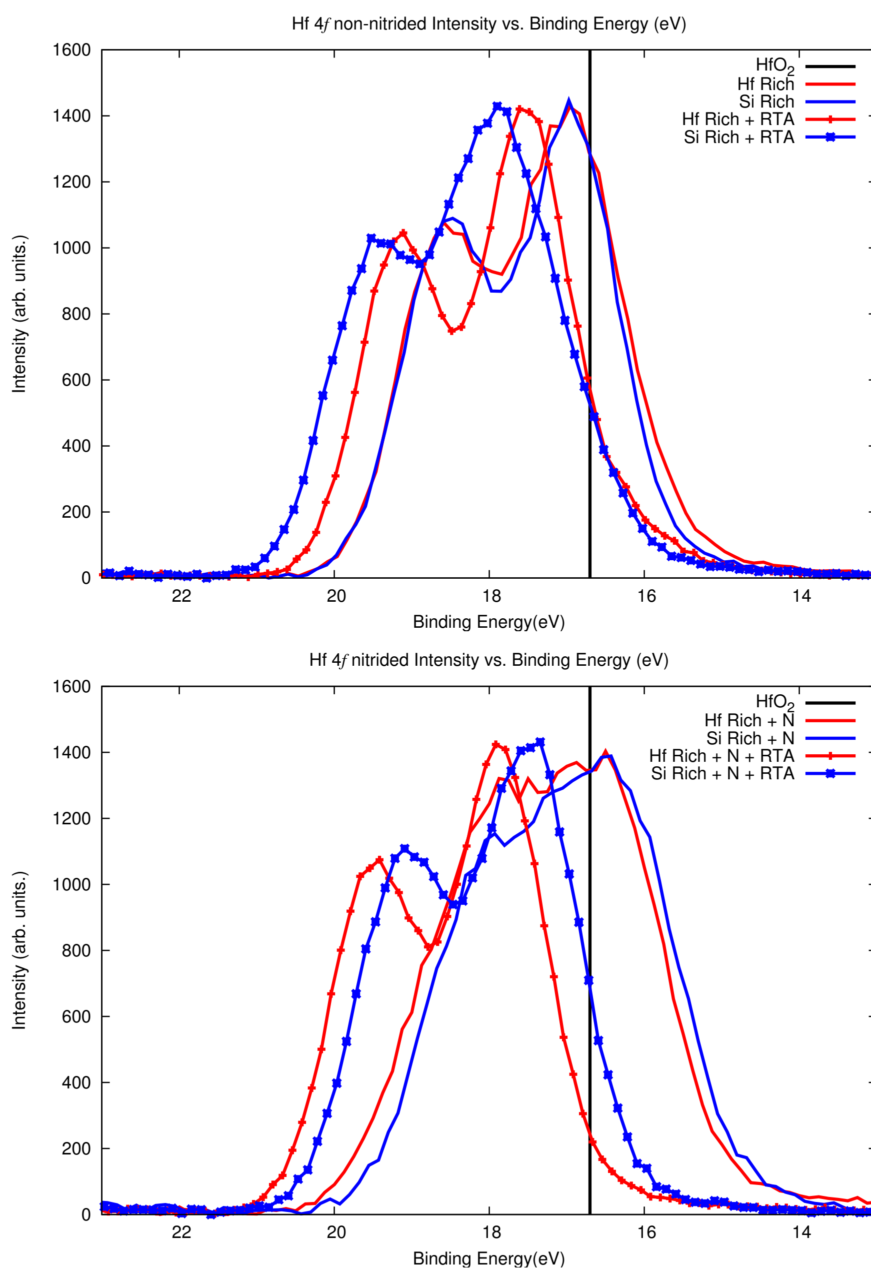

Figure 4.1: Hf 4*f* Binding energy for non-nitrided and nitrided hafnium silicates before and after rapid thermal annealing to 950°C for 10s. The intensities have been normalized for comparison purposes.

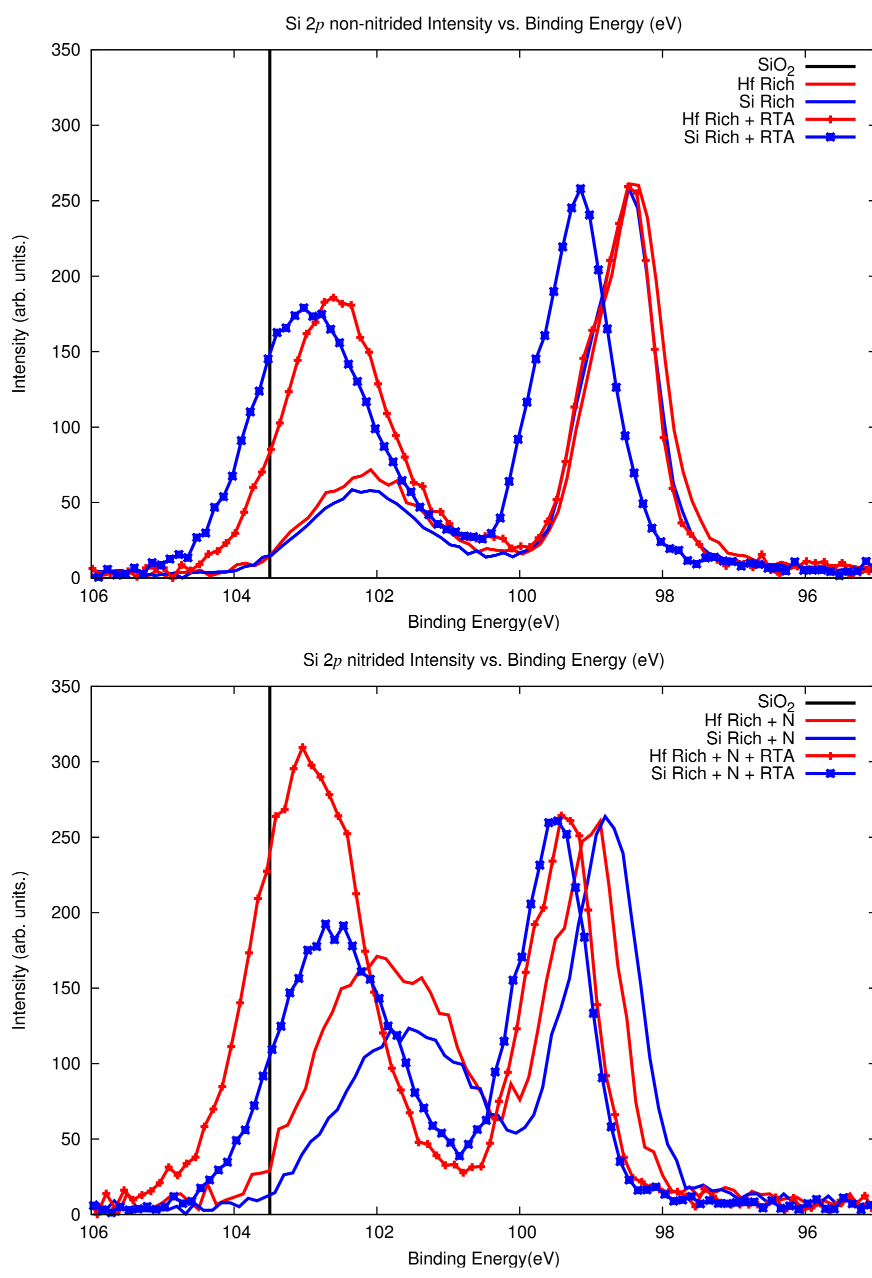

Figure 4.2: Si 2*p* Binding energy for non-nitrided and nitrided hafnium silicates before and after rapid thermal annealing to 950°C for 10s. The Si^0 2*p* intensities have been normalized for comparison purposes.

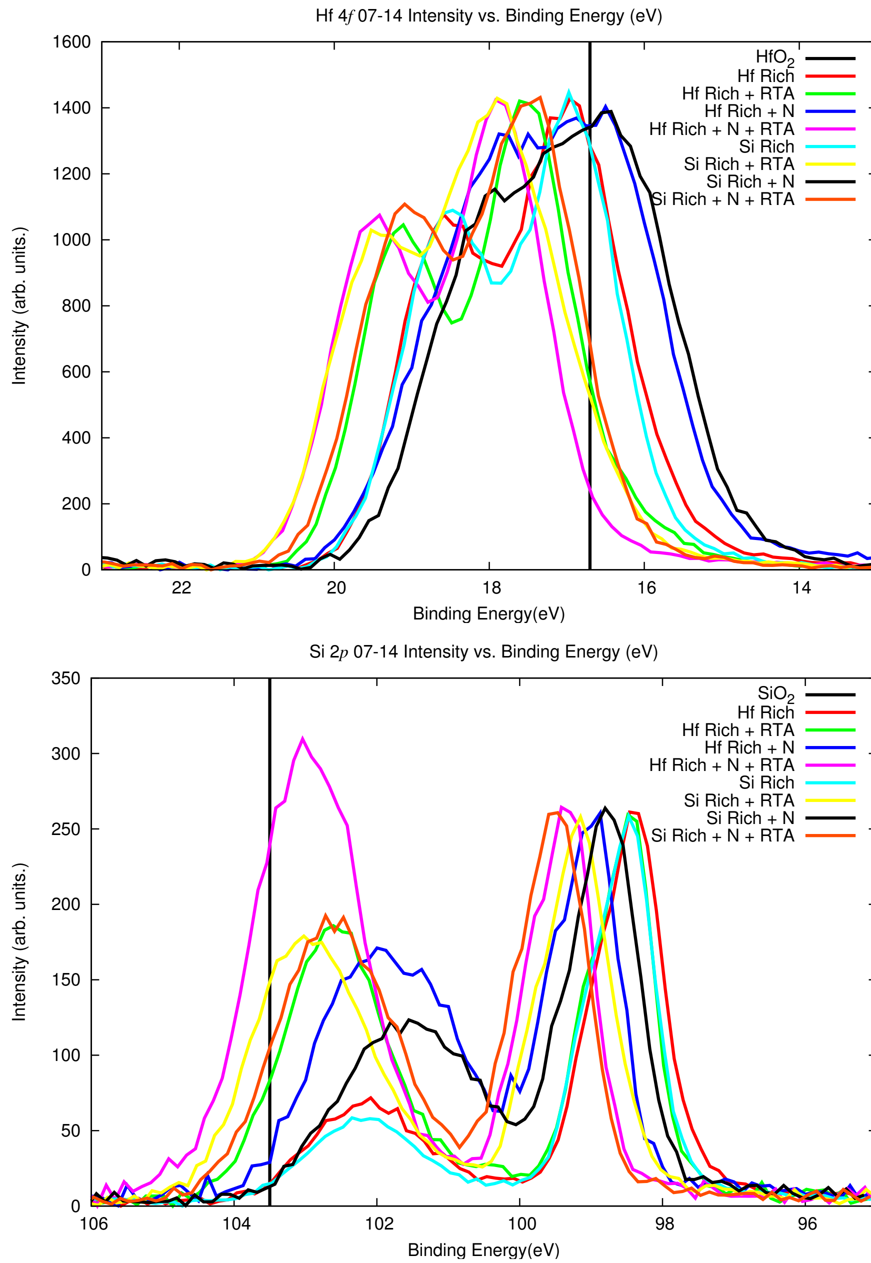

Figure 4.3: Hf 4*f* and Si 2*p* as a function of various processing conditions

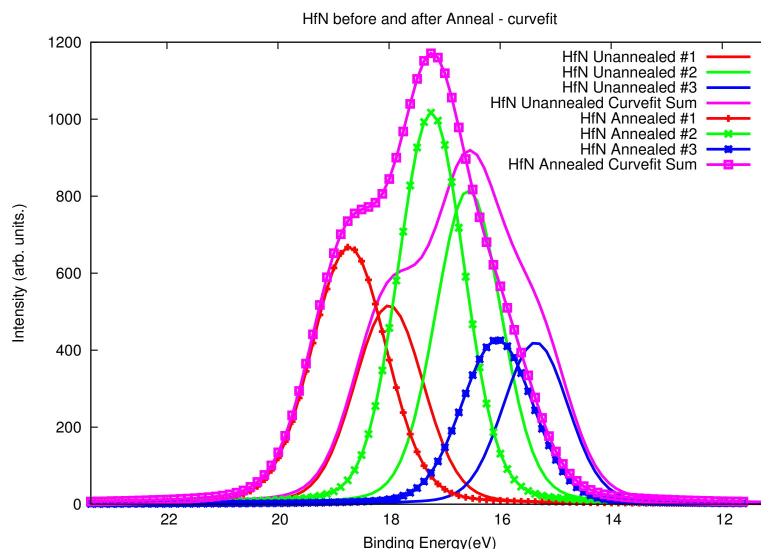

Figure 4.4: Hf 4*f* for a HfN sample prepared using ALD curvefit to three components, shown before and after anneal in vacuum to 600°C for 1 hour.

Treatment	C	N	O	Si	Hf
HfN as is	11	15	49	0	24
Hf sputtered 2 min	5	22	40	0	33
HfN sputtered 10 min	2	27	33	0	38
HfN sputtered 10 min and annealed 600°C, 1hr	3	23	38	0	36

Table 4.1: Atomic concentrations of the various elements in HfN varying with treatment.

4.1 Hafnium Nitride

Hafnium Nitride prepared using ALD was similarly experimentally investigated. An experiment involved the annealing of a hafnium nitride sample in vacuum. A shift towards higher binding energy was observed in this case as well. Figure 4.4 shows the curvefitted peaks (fitted to 3 gaussian components) shifting to higher binding energies with annealing. This could attributed to changes in interfacial charge with annealing.

Another experiment with HfN involved cleaning the surface of the HfN with an argon sputter. Because of carbon contamination as well as oxidation of the sample in the ambient, the composition of the sample was skewed towards showing lesser hafnium

than was actually representative of the film as shown in table 4.1. Sputtering it for 2 minutes brought down the oxygen and the ratio of Hf:N went up. With 10 minutes of sputtering, the composition was closer to stoichiometry. An annealing was done in situ after this, and the sample was seen to getter some more oxygen. From figure 4.5, the O 1*s* peak intensity comes down post sputter as expected, the peak is also narrower and better defined, possibly due to removal of the hydrocarbon contributions. The O 1*s* intensity goes up a bit after the anneal probably because of gettering effects.

More interestingly, Figure 4.6 shows the reduction of the higher binding energy shoulder on the hafnium with the removal of the oxygen species attached to it, and the increase of intensity. Annealing brings the Hf 4*f* peak higher in energy again possibly due to interfacial charge related dynamics. Once the adventitious carbon and other impurities are removed, the Hf signal intensity peaks. The Hf 4*f* has shifted to a lower binding energy after 10 minutes of sputtering with argon beam could be indicative of different local bonding state at the interior or sputter damage induced change. We can also notice an enhanced lower binding energy peak component here. Annealing at 600°C for 1 hour partly reversed that trend. The N 1*s* peak to start with has a sharp N-O bonding component at a higher binding energy. The cleaner surface after 2 minutes of sputtering has improved the amount of nitrogen seen. There seems to be no evidence of N-O bonding hereafter. At 10 min of sputtering the N seems bonded at higher BE though absence of C 1*s* referencing makes ruling out of charging effects difficult. As with the Hf, annealing restores the N 1*s* to roughly the earlier binding energy.

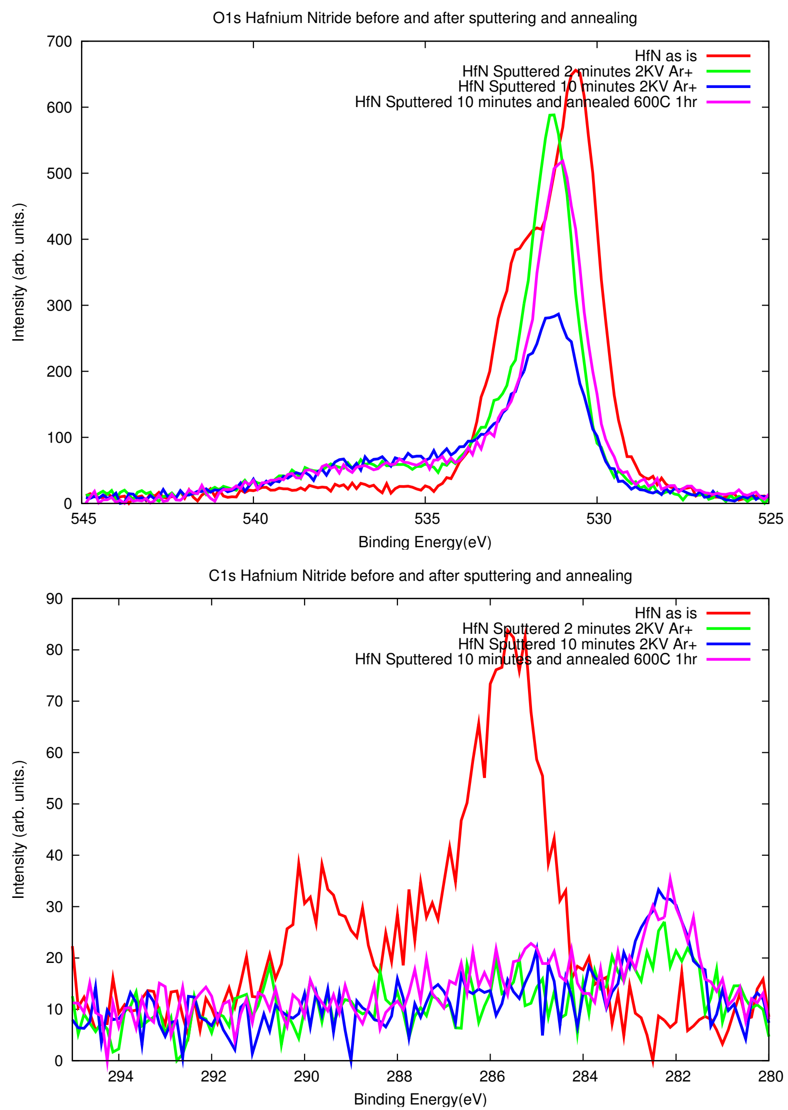

Figure 4.5: O 1*s* and C 1*s* for a HfN sample prepared using ALD shown before and after Ar^+ sputter followed by an anneal in vacuum to 600°C for 1 hour.

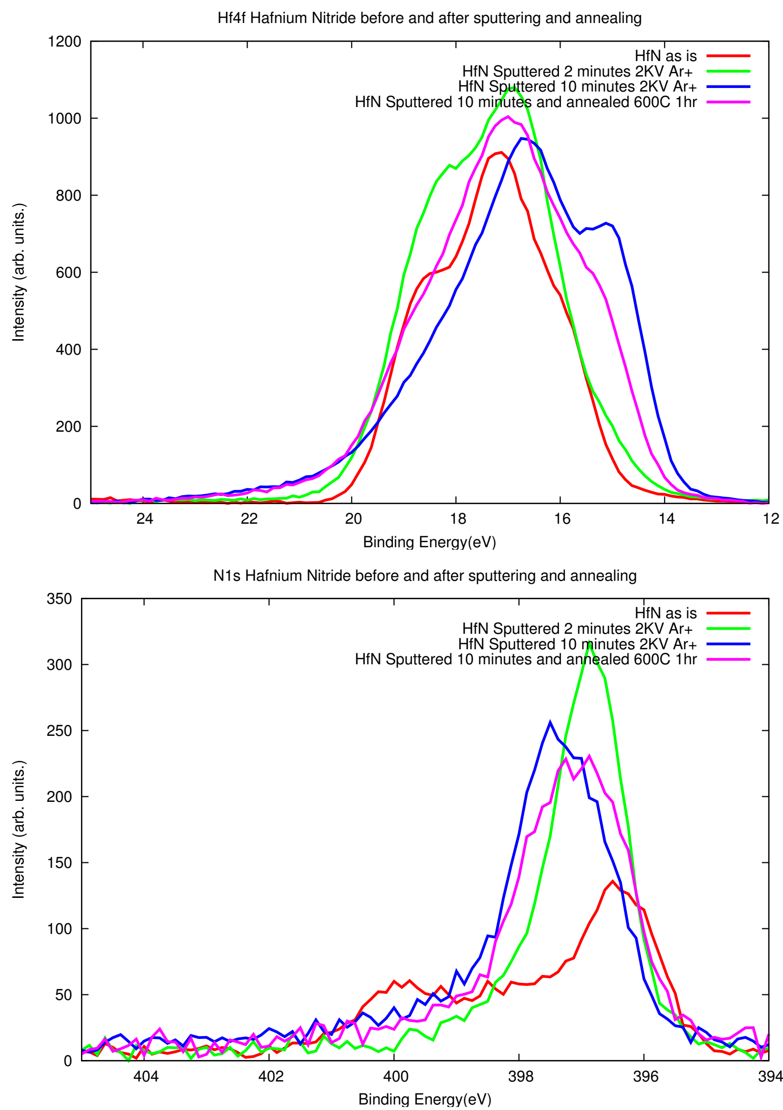

Figure 4.6: Hf 4*f*, N 1*s* for a HfN sample prepared using ALD shown before and after Ar^+ sputter followed by an anneal in vacuum to 600°C for 1 hour.

Chapter 5

MAXIMUM ENTROPY BASED DEPTH RECONSTRUCTIONS

5.1 Angle resolved photoemission

We can exploit the fact that photoexcited electrons can travel only a limited distance (typically two to three times the electron attenuation length) through the thin film. Tilting the sample relative to the detection position changes the path of the traveling photon to be restricted to sampling either longer distances near the sample surface or more through the bulk of the film. Thus, at glancing take off angles, photoemission spectra reflect only the composition of the surface layers while take off angles closer to normal incidence sample the specimen deeper. This is illustrated in figure 5.1

5.2 Maximum Entropy Algorithm

We utilize angle-resolved photoemission data in conjunction with a maximum entropy algorithm for converting angle dependent photoemission data into a concentration depth profile. Many algorithms for calculating concentration depth profiles from angle resolved photoemission spectra measurements have been published over the last decade, ranging from simple least-squares fitting to the Tikhonov regularization and maximum entropy methods[40]. Cumpson[40] reviews a variety of techniques and highlights the problems associated with reconstructing the depth profile from the angle resolved data, which is inherently an under-determined problem. Thus we seek to choose among many possible reconstructions by selecting those that minimize any artificial correlations in the

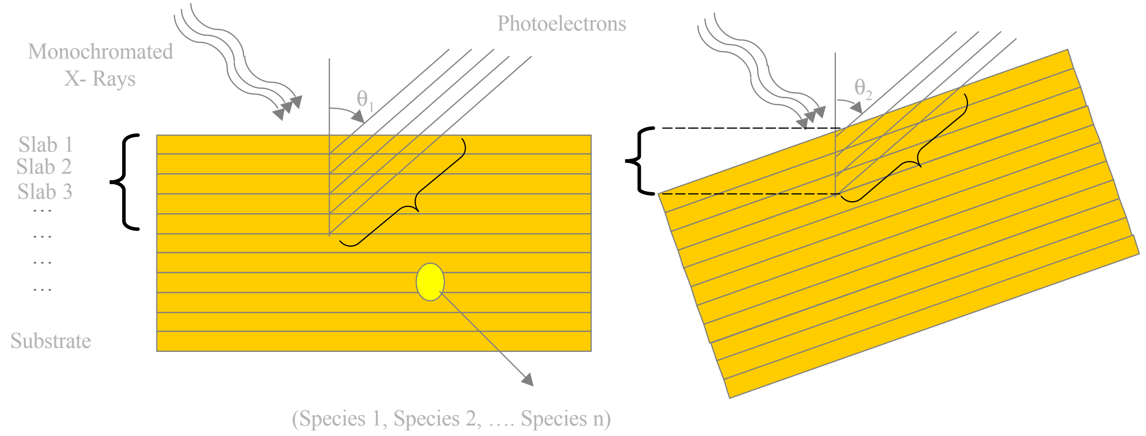

Figure 5.1: Angle resolved photoemission – illustration of how the sampled depth changes with angle

data and use minimal assumptions about the sample structure. This can be expressed mathematically as equivalent to maximizing a functional Q given by:

$$Q = \alpha S - \frac{\chi^2}{2} \tag{5.1}$$

where S is an informational entropic term that tracks deviations from an initial assumed profile and $C = \frac{\chi^2}{2}$ is a chi-squared term that measures deviations between the observed and calculated intensities.

The entropic term as shown by Gull and Skilling [41, 42] is given by:

$$S = -\sum_j \sum_i n_{j,i} - m_{j,i} - n_{j,i} \log(\frac{n_{j,i}}{m_{j,i}}) \tag{5.2}$$

where $n_{j,i}$ is the proportion of element j in the ith layer, $m_{j,i}$ is the initial estimate of the atomic fraction of element j in layer i;

$$C = \chi^2 = \sum_k \frac{(I_k^{calc} - I_k^{obs})^2}{\sigma_k^2} \tag{5.3}$$

where I_k^{calc} and I_k^{obs} are the calculated and observed photoelectron intensities at the kth measurement angle and σ_k^2 is the variance of the kth measurement. Fig. 5.2 summarizes the essential flow of logic for the maximum entropy program as it iterates over possible depth profile reconstructions to select the best one.

Figure 5.3 shows an example of how the maximum entropy based subroutine iterates from an initial depth profile reconstructed from one of the angles to a final profile. This is obtained by perturbing the concentration of the species one at a time in loops involving various slabs into which we divide the film, calculating the functional Q at each of these perturbed concentrations and allowing it to be maximized till we get a final converged profile. The film that is reconstructed here is a relatively hafnium rich hafnium silicate, ammonia nitrided at 800°C.

From the reconstructed depth profiles, we observe details that are in keeping with our expectations about the film. The carbon, mostly adventitious in nature is seen to be restricted to outer surface. The Hf^{4+} and the Si^{4+} concentrations are seen to be roughly constant throughout the film. The interface appears to be SiO_2 given the increasing concentration of oxygen there. The nitrogen is observed to be deep within the film relative to the oxygen. Of interest is the double humped nature of the oxygen depth profile. This is to be expected, since the surface is oxidized and the dielectric silicon interface appears to be SiO_2 as well.

Some of the limitations to the conclusions we can draw from this are seen from the broad interfaces that seem to be inherent in the way the program works. The concentrations depend upon sensitivity factors that need to be calibrated well for best results using data from other techniques such as Rutherford backscattering. Obtaining good depth calibration is also dependent upon accurate electron attenuation lengths. Further work in this direction is being explored with studies of reconstruction of hafnium silicate films with an implementation of the maximum entropy method using the Bryan Algorithm [43].

Figure 5.5 plots the Oxygen (Red) and Nitrogen (Blue) profiles as well as the

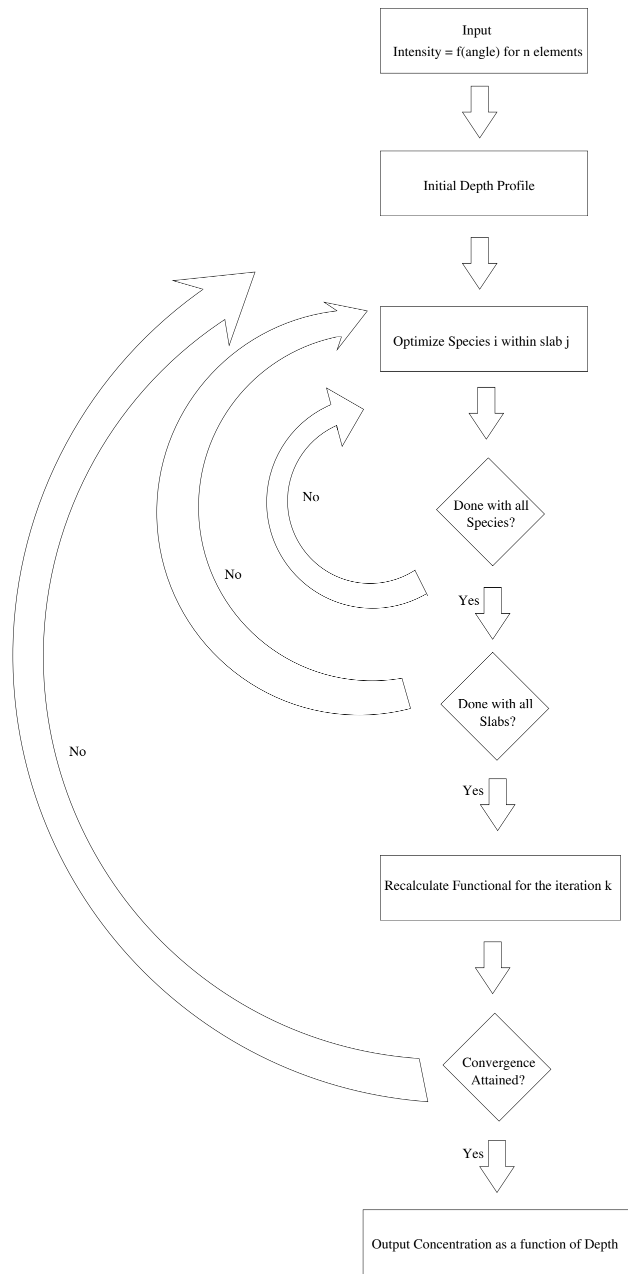

Figure 5.2: Flow Chart outlining the program flow for depth profiling of the hafnium silicate using a maximum entropy algorithm

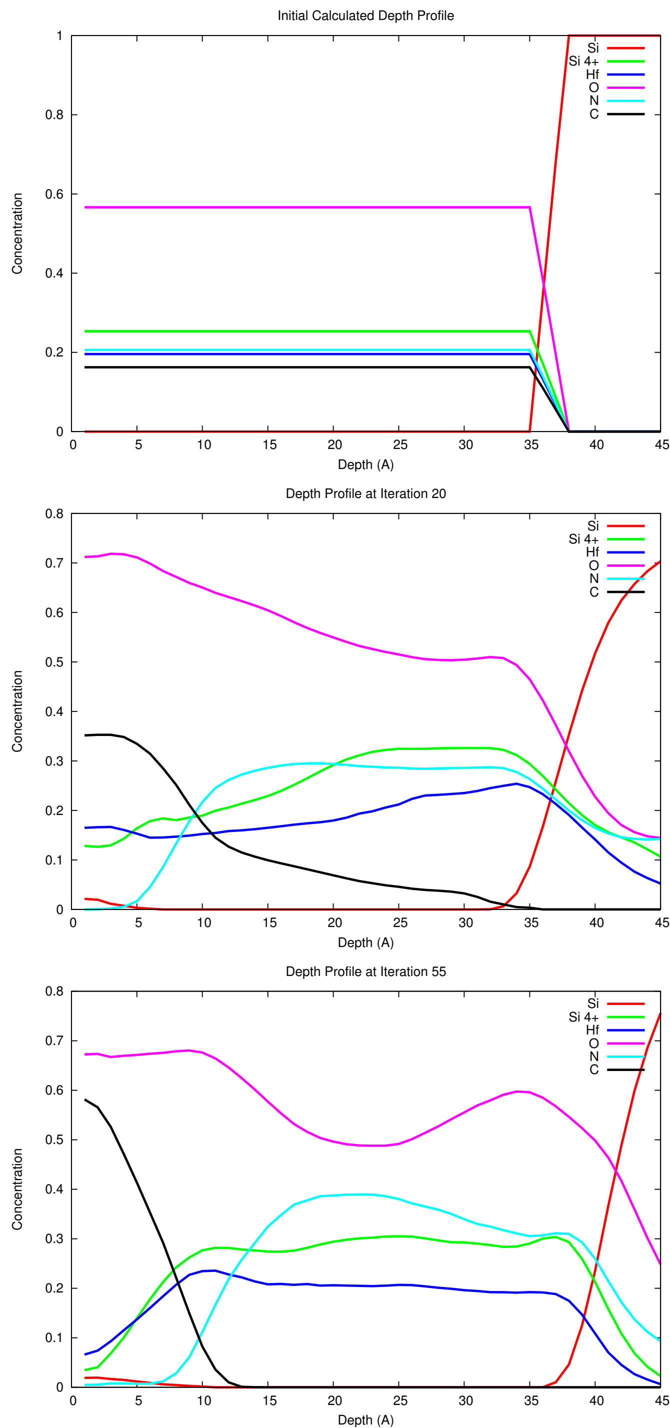

Figure 5.3: Evolution of the depth profiles for a hafnium silicate sample from the initial assumed profile (top) to the finally converged profile (bottom)

position of the silicon substrate (Black) for three ALD deposited hafnium silicate films thermally nitrided with ammonia at three different nitridation temperatures, 700, 800 and 900°C. The lowest temperature is designated with the solid data points, the medium temperature with the half shaded data points, and the highest temperature ones with the hollow data points. From the figure, we can infer a progressive trend with increasing nitridation temperatures that shows relatively decreasing oxygen concentrations and a correspondingly increasing nitrogen concentration. This trend seems to suggest that there is a substitution of oxygen atoms with nitrogen atoms as we nitride it at progressively increasing temperatures, and the nitrogen profile in this particular set of films seems to be directed closer to the stack than to the surface. Note especially, how at the highest temperature, the relative concentrations of nitrogen is actually higher than that of the oxygen, (the pair being indicated by the dotted line joining them) as opposed to the two lower nitridation temperatures at which the oxygen concentrations are always dominating the amount of nitrogen present in the film. As a test of validity, consider the metric 2[O]+3[N], where [O] and [N] are the integrated areas of oxygen and nitrogen respectively under the depth profile concentration, and the constants 2 and 3 refer to the number of nearest neighbors that the they bond to. As seen from figure 5.4, this metric is seen to remain approximately constant for the three reconstructed depth profiles for samples processed at three different nitridation temperatures, suggesting the consistency of the processed data and validating our conclusion regarding the replacement of oxygen with nitrogen atoms. This kind of non-destructively obtained concentration depth profile data is thus useful to make out trends that can then be correlated to film deposition techniques and resulting device properties.

5.3 Comparison of Maximum Entropy with MEIS Data

Medium Energy Ion Scattering (MEIS) was employed to analyze the composition depth profile of one of the films that was relatively silicon rich and ammonia nitrided at 800°C. The maximum entropy reconstructed output was rescaled in the terms of depth

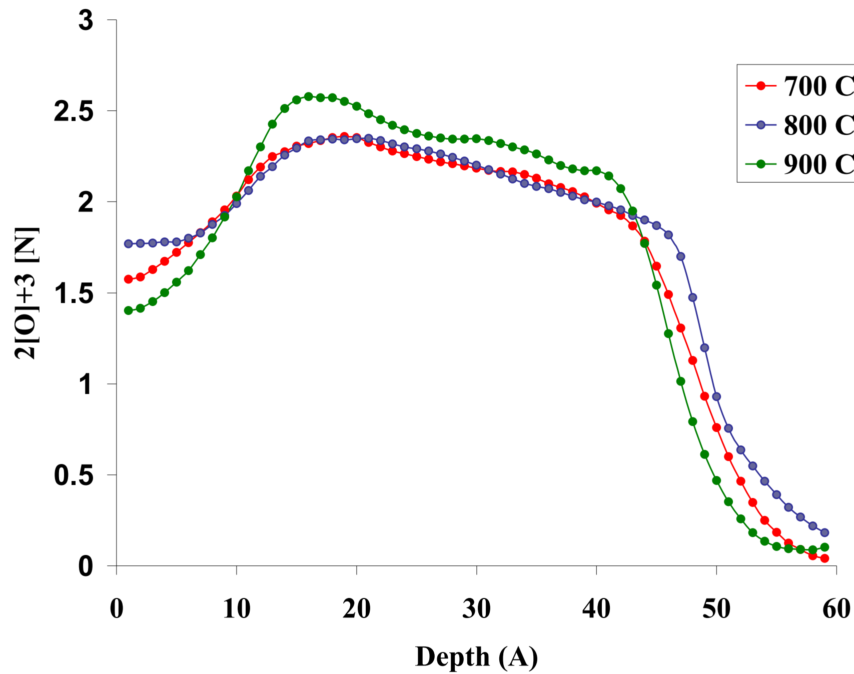

Figure 5.4: The metric 2[O] + 3[N] plotted for reconstructions obtained at three different temperatures is seen to remain roughly constant, suggesting consistent results.

obtained from the MEIS results and the two data sets were superimposed (Figure 5.6). The agreement is reasonable, and gives a good sense of the utility of the program. This also gives a good way to calibrate the atomic sensitivity factors which are crucial to getting the right depth scales using the maximum entropy program.

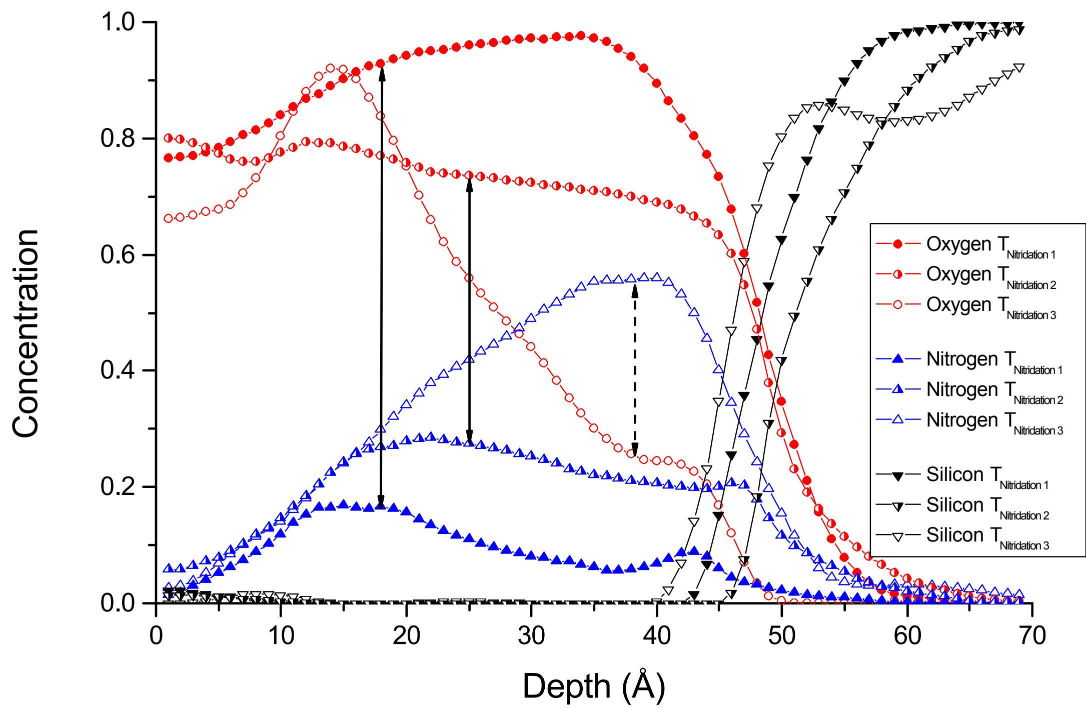

Figure 5.5: Trends in oxygen versus nitrogen profiles for three hafnium silicate films nitrided at different temperatures as reconstructed by the maximum entropy method. The oxygen appears to be substituted by nitrogen at progressively higher temperatures.

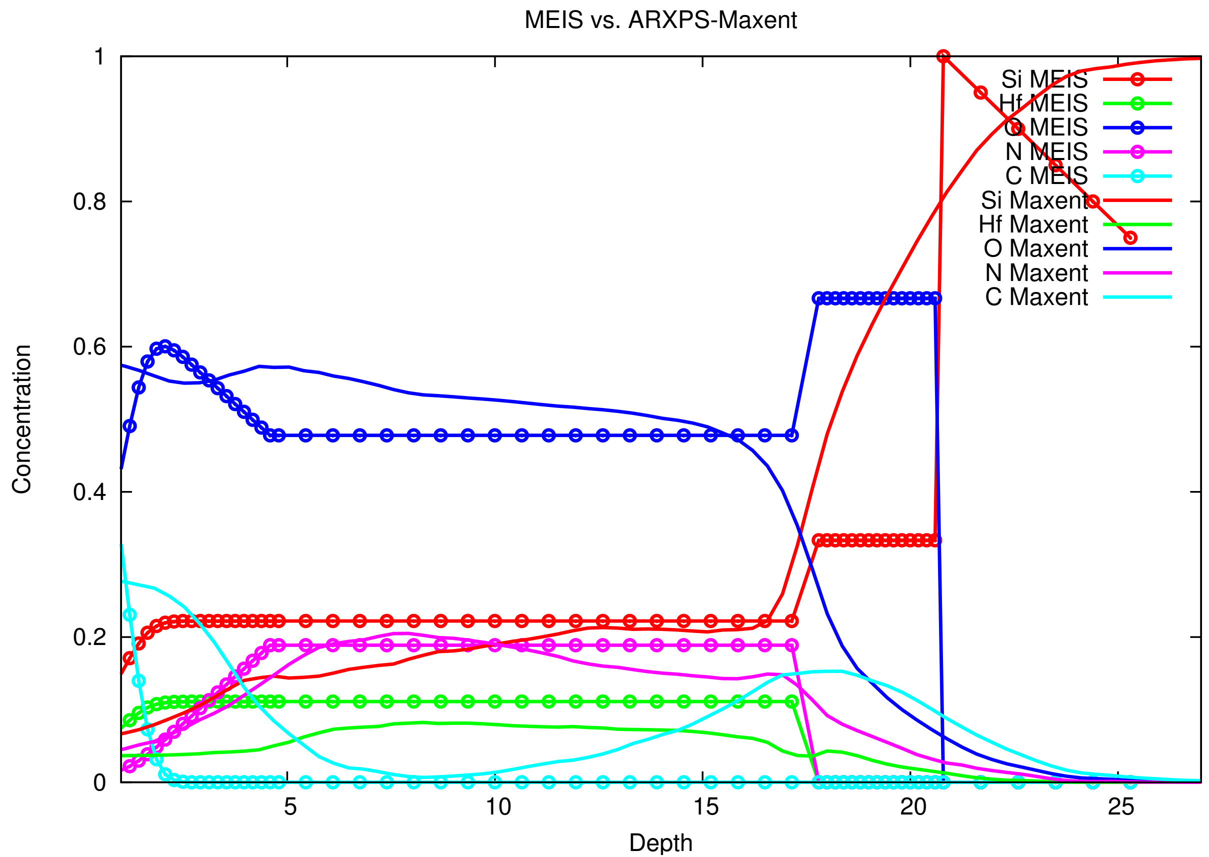

Figure 5.6: Comparison of MEIS data and maximum entropy generated depth profile data.

Chapter 6

VALENCE BAND SPECTROSCOPY STUDIES OF TIN/TA$_2$O$_5$ TIN/Al$_2$O$_3$ INTERFACES

6.1 Synchrotron Radiation

Synchrotron radiation is a good source of ultraviolet photons that can be used for studying the valence band edge of titanium nitride and its interface with insulating oxides such as Ta_2O_5 and Al_2O_3 which are being studied for metal-insulator-metal (MIM) capacitor applications. The samples were prepared using Atomic Layer Deposition at ASM America, Inc. Ultraviolet radiation, being lower in excitation energy (∼10–45 eV) compared to the X-rays used in X-ray photoemission (∼1400 eV) has a greater cross-section / sensitivity at the valence band edge. Synchrotron radiation has greater photon flux than conventional alternatives for ultraviolet (UV) radiation and also allow us to tune the energy.

Experiments were performed at the U4A beamline at Brookhaven National Labs.

6.2 Beamline Characteristics

Of the choice of three gratings available at U4A, grating 3 was chosen which has 300 lines/mm and is suitable for tuning in the energy range 10-80 eV. It has a resolution ($\frac{dE}{E}$) of 2×10^{-4}, and a flux around $4 \times 10^{10} \frac{ph}{sec(0.1\%bw)}$ (at 500 mA)

The source of the radiation is a bending magnet located upstream. The beamline Optical System consists of two mirrors and a monochromator. Mirror 1 is a gold-coated glass toroidal mirror (M0), $4.325°$ grazing angle of incidence, 22.5 mrad horizontal collection angle, and focuses at sample position in upstream endstation.

The beamline uses a spherical grating monochromator (SGM), with $162°$ included angle, 2 m entrance armlength, and 4.0–4.4 m (variable) exit armlength. The entrance slit is located 2.45 m downstream of the M0 mirror. The three spherical gold-coated ultra low expansion (ULE) gratings are interchangeable in UHV.

Mirror 2 is a refocusing mirror, a gold-coated glass toroid, at $4.675°$ grazing angle of incidence, providing horizontal and vertical focusing of beam.

6.3 Experimental

The samples were scanned using 29.7 eV incident energy. A -9.0 V constant bias was applied to the sample to impart an excess kinetic energy to the electrons as to make the secondary cutoff and other features clearly evident. Spectra were accumulated at the valence band edge and the secondary electron cutoff for various samples. The information from this can be translated into a band alignment picture as discussed below (summarized in figure 6.6).

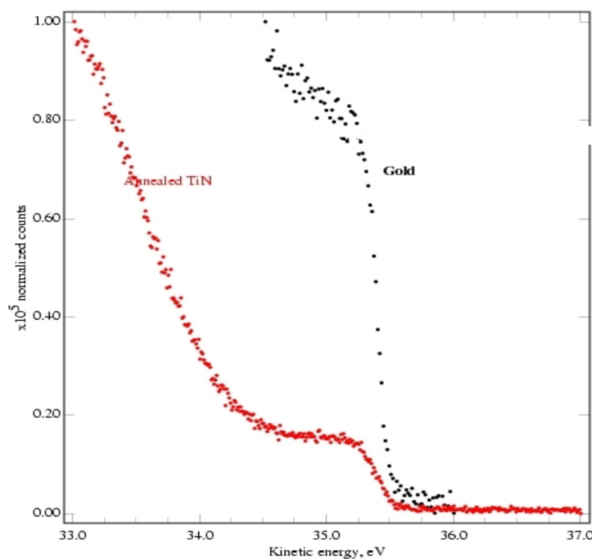

Figure 6.1: Au and TiN Fermi Edges

The gold and the titanium nitride Fermi edges roughly match up (See Figure 6.1). Gold being more metallic in character has greater density of states at the Fermi level indicated by greater intensity at the Fermi energy. This energy has been roughly measured to be 35.5 eV kinetic energy from the plot. Not surprisingly, the Fermi edge for both samples is found at the same energy as both samples are connected to ground in identical electrical circuits.

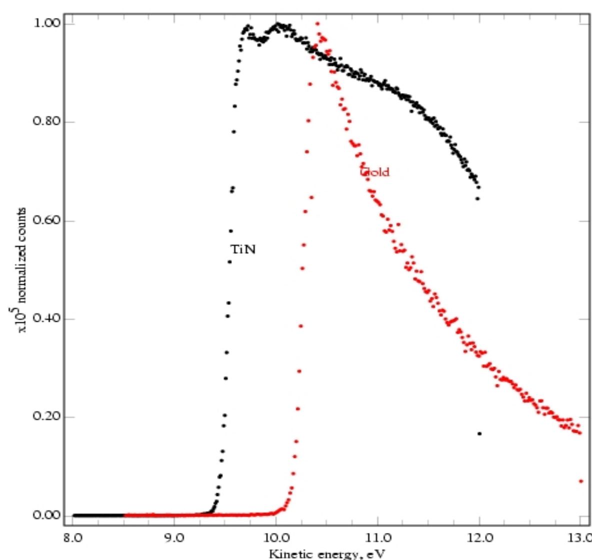

Figure 6.2: Au and TiN secondary electron cutoffs

The secondary electron cutoff is the abrupt fall off in the intensity at the lower kinetic energy side of the photoelectron spectrum, where the electron that is being probed no longer has sufficient kinetic energy to overcome the work function of the surface (See Figure 6.2). The intensity at the secondary electron cutoff is rather high because of the large proportion of photoexcited electrons that undergo scattering events and lose substantial kinetic energy before leaving the surface. In terms of the energy distribution, the intensity background keeps increasing from the high kinetic energy side to the low kinetic energy side due to progressively increasing number of scattered electrons. The secondary electron cutoff essentially defines the vacuum level of the system (which is defined as the

point where the electron has zero kinetic energy). From the position of the Fermi edge and the secondary electron cutoff we can thus calculate $\Delta\phi$.

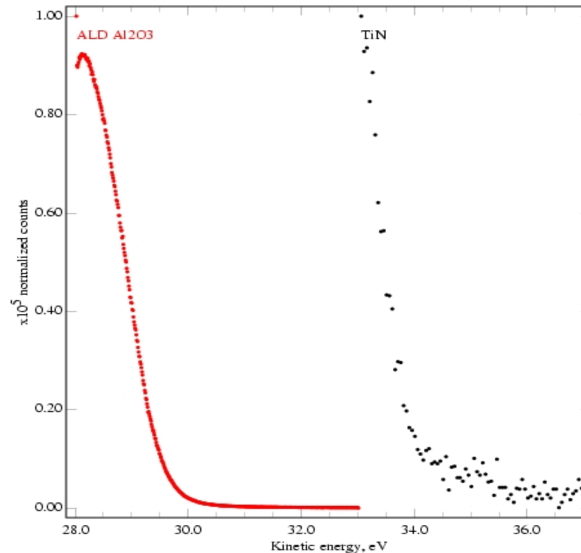

Figure 6.3: ALD Al_2O_3 and TiN Fermi Edges

Once insulators such as Al_2O_3 or Ta_2O_5 are deposited on the TiN, they no longer have electron density at the Fermi level because of the band gap between the valence and conduction band. So essentially, we can compare the top of their valence band with the Fermi edge of the material on which they are overlaid. This is the basis of the basic band alignment picture. If we know the band gap of the material we can extrapolate the bottom of the conduction band from the valence band energy as well. An optical band gap measurement should be sufficient for these samples. The current band alignment picture is computed using the values of band gap obtained from literature.

6.4 Band Alignment

From the positions of the valence band edges with respect to the gold Fermi level and data from the secondary electron cutoffs, we can reconstruct a picture of the relative band alignment of the various materials with respect to each other. From the schematic,

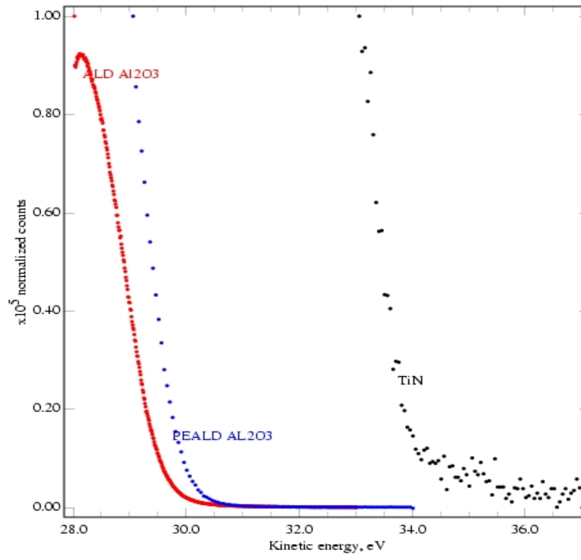

Figure 6.4: PEALD Al_2O_3 and TiN Fermi Edges

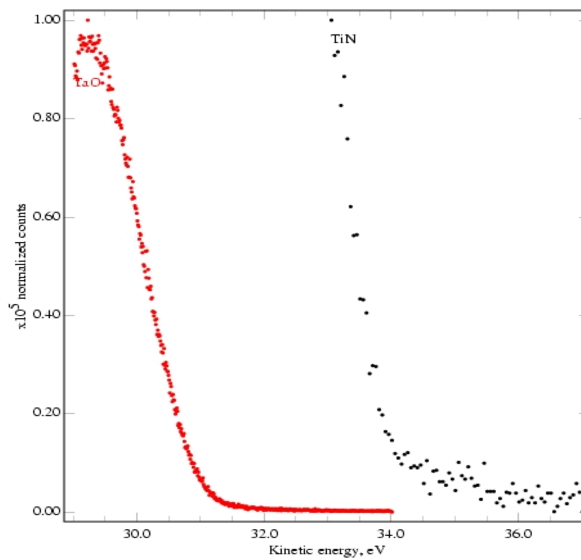

Figure 6.5: Ta_2O_5 and TiN Fermi Edges

Ta_2O_5 has a very small offset in energy between the Fermi level of the TiN and its conduction band, so some asymmetric leakage current in one direction of bias might be expected in an I-V measurement. The numbers need to be refined further for accurate positioning

of these bands.

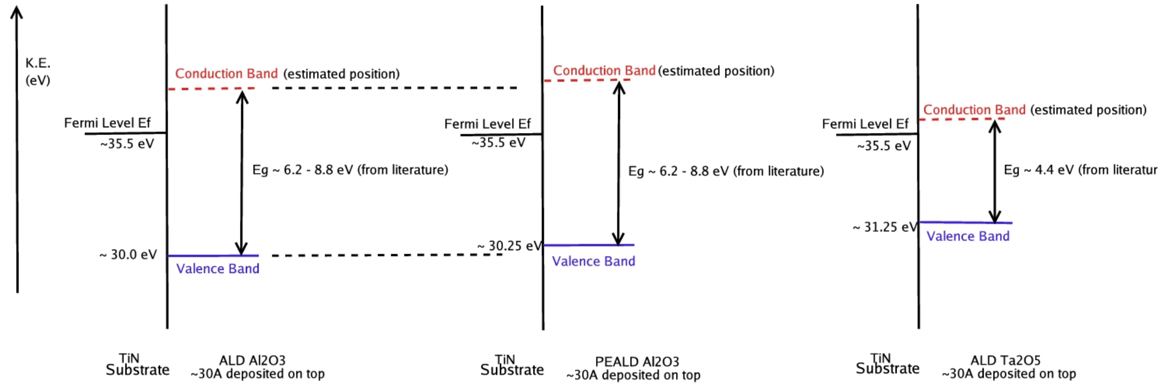

Figure 6.6: Band Alignment

6.5 Future Experiments — Metal Gates for transistors

An extension of the band alignment studies of MIM capacitor studies would be metal gates for next generation CMOS applications.Heavily doped poly-silicon has been traditionally used as the 'metal' in the transistor CMOS capacitor because of processing compatibility with the materials involved. However, its deficiencies are pronounced as we move towards thinner dielectrics such as its lack of sufficient charge carriers in spite of heavy doping[44, 45]. Polysilicon shows depletion at the dielectric interface when the transistor channel is in inversion. This limits the inversion capacitance that is required. The higher poly doping levels that will then be required according to the ITRS roadmap[46] may not be feasible. Thus the high poly-silicon resistance limits the drive current, and hence metal gates would help relax the requirements for high-κ inversion capacitance requirements and boost transistor performance. Eliminating poly-silicon has other advantages such as eliminating the need for a poly thermal activating step, thereby allowing the thermal processing to be optimized for source-drain engineering exclusively. The downside is the need to engineer the work function of the appropriate metals for NMOS and PMOS and the much more complicated processing.

An extension of this study would thus involve interrogating the interfaces of high-κ materials such as hafnium silicates with alternative metal electrodes such as ruthenium, titanium nitride, tantalum, etc. The various factors studied will include band alignment studies using photoemission, using soft synchrotron X-ray photoemission. Various processing parameters that might be expected to influence differences in this include differences caused due to plasma vs. thermal processing. The degree of Fermi level pinning[45] of metal/dielectric interface for different metalizations is also to be investigated. The presence of interfacial charge in the resulting metal-dielectric interface would also be interesting to investigate using photoemission.

Chapter 7

PHOTOEMISSION STUDY OF MAGNETIC TUNNEL JUNCTION INTERFACES

7.1 Magnetic Tunnel Junctions

Magnetic Tunneling Junctions (MTJ's) constitute an important technology that is important to the development of magnetic random access (MRAM) memories and other spin electronic devices[8, 9, 10]. Of particular interest to the current study is the study of the FeNi/Al_2O_3/FeNi and Co/Al_2O_3/Co MTJ which poses several interesting questions such as the presence of charge accumulation at FeNi/Al_2O_3 or Co/Al_2O_3 interface and the interfacial chemistry associated with such systems. X-Ray Photoelectron Spectroscopy can be used to characterize the compositional, chemical, and electronic properties of this system, which can then be correlated to various other properties of this interface, such as magnetoresistive properties.

The MTJ stack involves two magnetic layers separated by a thin dielectric barrier (Figure 7.1). The direction of magnetization of one of the magnetic layers need to be in a fixed direction. The direction of polarization the free magnetic layer is the basis for information storage. The resistance of the stack switches between a low or a high state depending on the relative polarization of the free layer versus the pinned layer – whether it is parallel or antiparallel. An external field is used to switch the direction of magnetization of the free layer to correspond to these two states.

Meservey and Tedrow [47, 48, 49] discovered Spin Polarized Tunneling, laying the basis for the whole field. The mechanism of Tunneling Magnetic Resistance (TMR) can

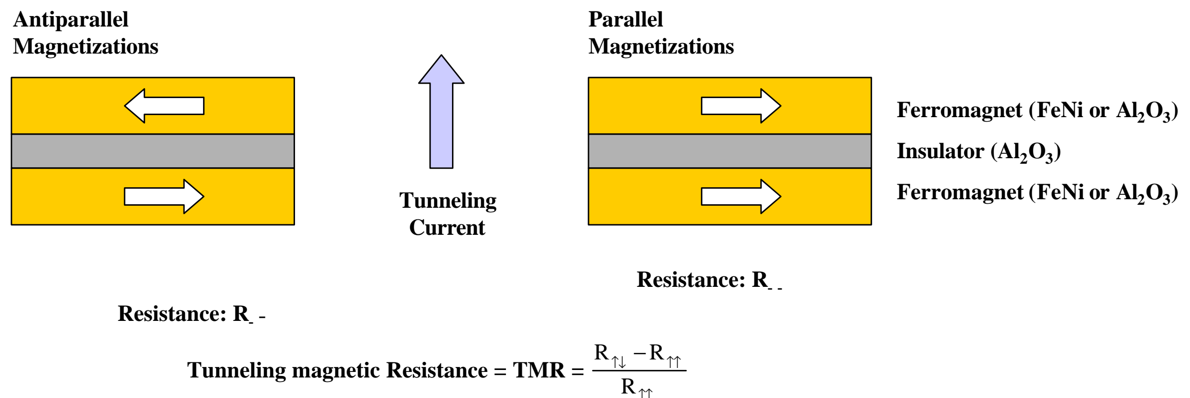

Figure 7.1: MTJ Schematic

be understood as a two-band model involving the d-band split into spin-up and spin-down bands with different densities of state at the Fermi energy. In the case of parallel magnetization of the layers, the majority-band electrons can tunnel across to the corresponding majority band of the opposing electrode and similarly for the minority bands. When antiparallel, the majority band electrons are forced to tunnel into the minority band of the opposing electrode and vice-versa. This reduces the number of states available for tunneling between layers in the antiparallel setup resulting in an increased tunneling resistance and is exploited for bit storage. More realistically, the barrier material also plays an important role in both the magnitude and sign of this effect. The tunnel barrier is very thin and the tunneling resistance is exponentially dependent on its thickness. Thus, the insulating barrier needs to be smooth, free of pinholes and very uniform over the wafer.[50, 51, 52, 53] The tunneling MR ratio is defined as the ratio of the difference in resistance between the high and low state and the resistance in the low state[54]. Jullière[55] made the first reported magneoresistance measurement on an Ferromagnet/Insulator/Ferromagnet trilayer junction and interpreted it. His model is still reasonably good in predicting the TMR on clean junctions.

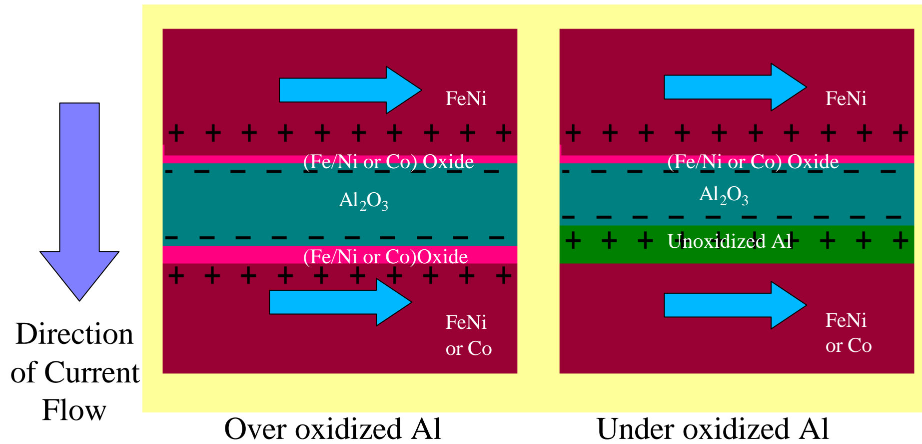

Figure 7.2: MTJ Underoxidized vs Overoxidized illustrating how the degree of oxidation of the aluminum barrier can be expected to affect the properties of the system.

Application for Magnetic Tunnel Junctions include non-volatile memory elements (MRAMs) and magnetic sensors. There are several features that magnetic tunnel junctions have that make it very attractive for these applications including their intrinsic high resistivity, low power consumption, high relative change in resistance ($\frac{\Delta R}{R}$), small dimensions allowing high densities, expected thermal robustness, radiation resistance and fast response.

7.2 Sample Preparation

Samples were prepared by the John Xiao group[56] at the University of Delaware. DC Magnetron Sputtering was employed to deposit the thin film layers with base pressures better than 3×10^{-7} Torr. Sputtering was done at 4.0 mTorr of Ar pressure. An Al film $\sim$ 10 Å was deposited at the junction. Al_2O_3 was produced by RF plasma oxidation with 60 mTorr O_2 partial pressure. The antiFerromagnetic layer of FeMn was deposited at 30 Oe magnetic field. The resulting film structure is represented schematically in figure 7.3

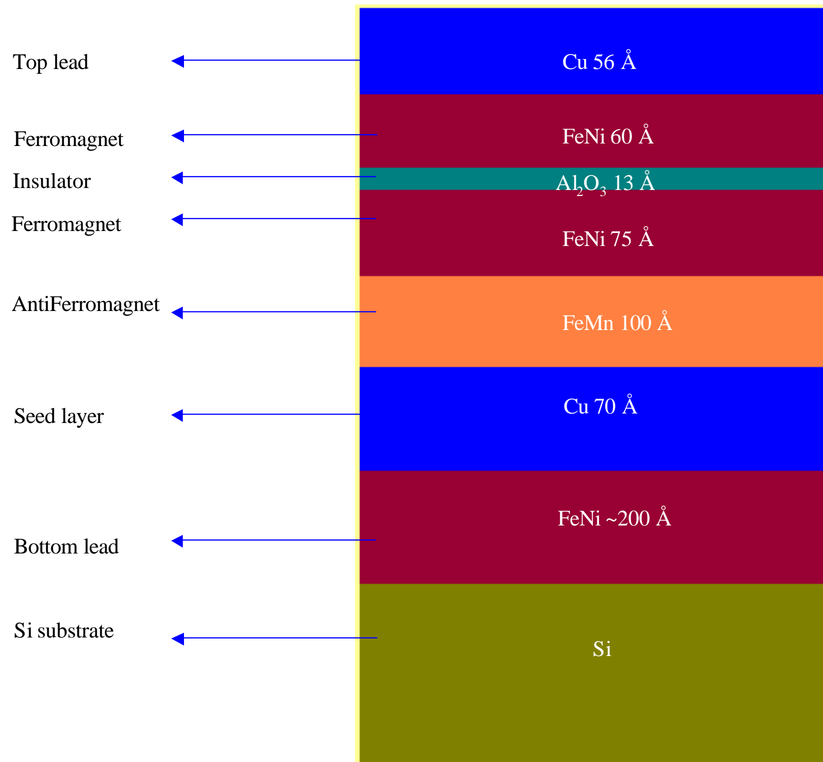

Figure 7.3: MTJ Layer Scheme for a FeNi/Al_2O_3/FeNi setup

7.3 Auger depth profile

The compositional variation as a function of depth was verified using Auger electron spectroscopy, and agrees well with the expected compositional distribution. The result is plotted on figure 7.3

7.4 XPS Results

Argon Sputtering was employed to systematically remove the film and a photoelectron spectrum was collected at fixed intervals for a Co/Al_2O_3/Co magnetic tunnel

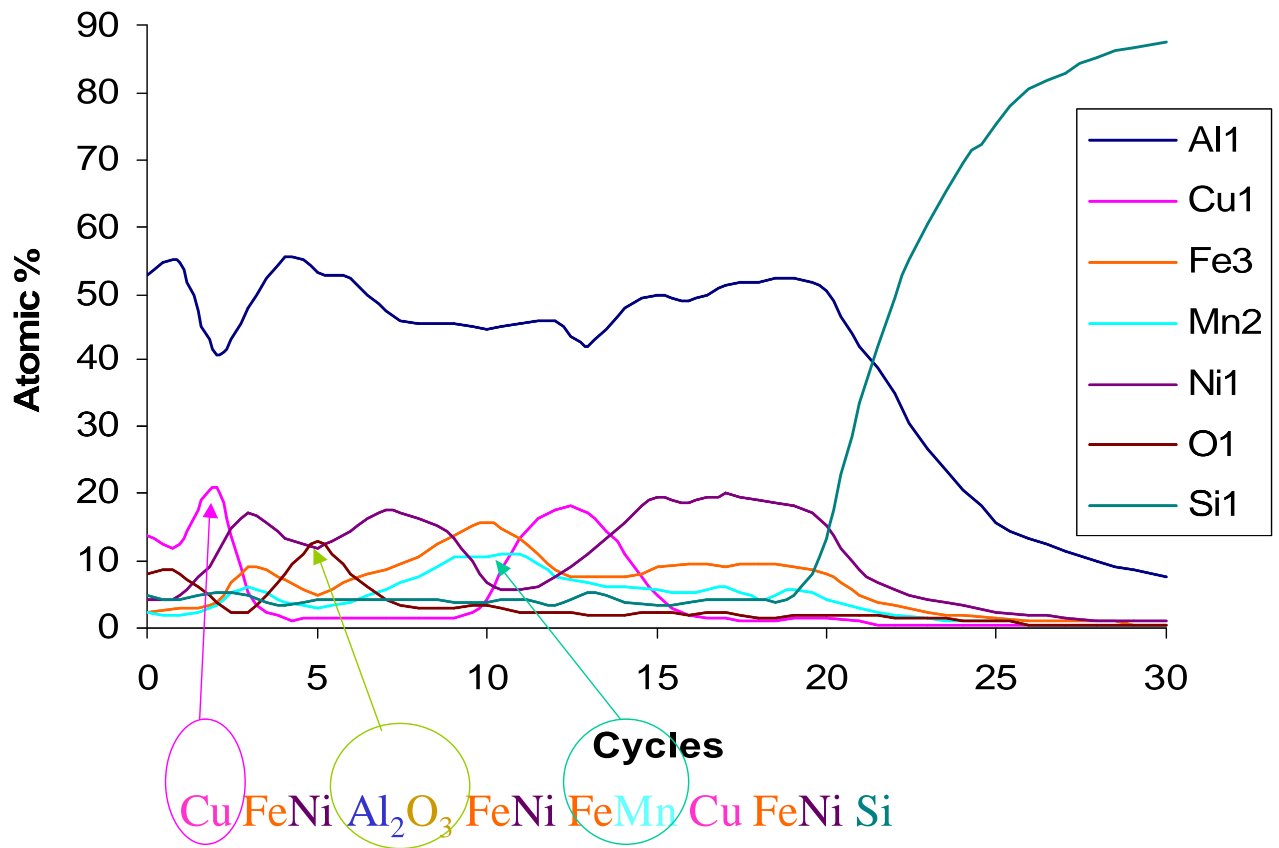

Figure 7.4: Auger Depth profile for a FeNi/Al_2O_3/FeNi MTJ sample validating the compositional depth profile of the film.

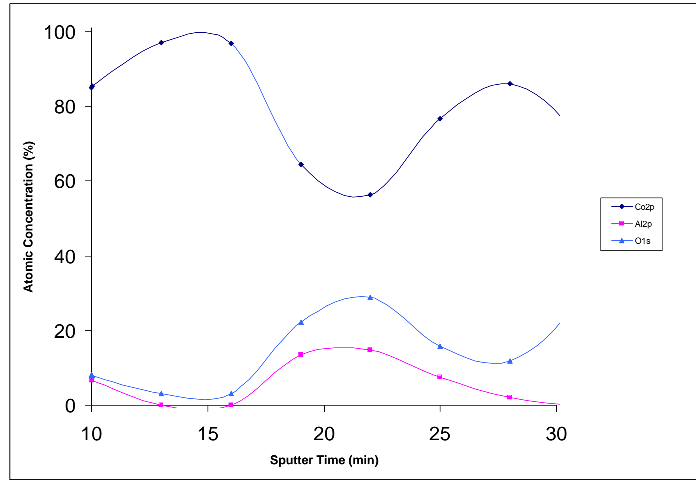

Figure 7.5: Depth Profile showing Al_2O_3 in a Co(160Å) / Al-oxide(10Å) / Co (85Å) / FeMn (85Å) /Cu (72Å) /FeNi (215Å) / Si structure.

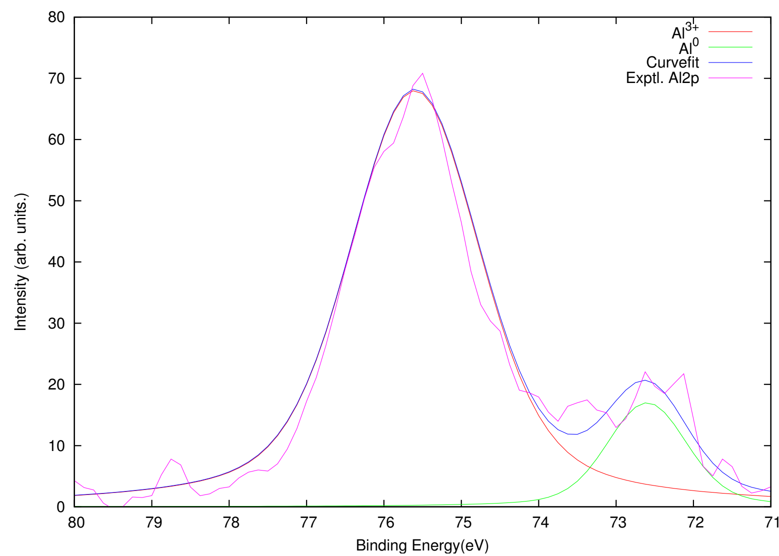

Figure 7.6: Photoemission peak of the oxidized Al_2O_3 peak showing its peak energy at a binding energy higher than 74.4eV, expected for Al_2O_3.

junction (instead of the FeNi/Al_2O_3/FeNi MTJ scheme earlier). The relevant portion of the spectrum is shown in figure 7.5 (The complete structure corresponds to Co(160Å) / Al-oxide(10Å) / Co (85Å) / FeMn (85Å) /Cu (72Å) /FeNi (215Å) / Si). The peak energy of the aluminum (figure 7.6) is shifted to a higher binding energy, possibly indicating the accumulation of interfacial charge. The quantity of this charge can presumably be correlated to the level of over or underoxidation of the aluminum layer as illustrated in figure 7.2. Quantifying the amount of this charge remains a work in progress. Opila *et. al.*[16] have estimated the interfacial charge in a comparable system as summarized in equation 9.1.

Chapter 8

PHOTOEMISSION EXPERIMENTS COMPLEMENTING THE STUDY OF COPPER ION TRANSPORT IN SIO_2 DIELECTRICS

8.1 Introduction

Diffusion barrier layers are used to prevent the migration of copper into active device regions and the associated degradation of the dielectric properties of the insulator in course of the integration of copper interconnects with silicon based microelectronics[11]. Due to the relatively high electrical resistivity of these barrier layers, it is desirable to scale the barriers to be as thin as possible[12]. The thickness scaling has lead to a need for a better understanding of the mechanism of copper transport through dielectric layers[13].

Investigations of copper transport in the SiO_2 dielectric have noted the influence of the oxygen ambient on the observations.[57, 58] Recent investigations of the transport mechanism have observed that copper transports as an ion in SiO_2 dielectrics, and that the copper ions originate from copper oxide layers at the electrode formed in the presence of oxygen. In contrast, Miyazaki *et al*[59] observed evidence of copper transport for samples furnace annealed in an inert gas ambient at 600°C for 1 hour, and Braud *et al*[60] reported copper transport for thermal annealing at 500°C in high vacuum. As part of an effort to better understand the mechanism of copper ion transport, Willis *et al*[14] investigated the role of oxygen partial pressure and its effect on copper ion transport rates in SiO_2 dielectrics. We provided photoemission data to complement these studies to identify oxidation states of copper in the films.

8.2 Experiment

Samples were prepared by Laura Parrish at the Brian Willis Group at the University of Delaware. Thermally oxidized copper samples and reactively sputtered copper oxide samples were grown or deposited onto p-type Si(100) wafers (1-10 Ω-cm) with a 100 nm thermal SiO_2 layer; patterned into MOS capacitor structures; and probed under vacuum and controlled oxygen ambient at elevated temperatures, and with electrical bias applied. Thermally oxidized Cu_2O and CuO samples were prepared by oxidizing patterned metal capacitors in-situ in the electrical probe station. Prior to oxidation, the metallic copper layers were deposited by DC magnetron sputtering, and the thickness was measured to be 100-150 nm by surface profilometry. Oxidation was carried out in the electrical probing apparatus with research purity oxygen at temperatures of 525-625K and oxygen partial pressures of 1-100 torr in a constant flow of oxygen. Reactively sputtered CuO films were deposited by RF sputtering of a CuO target in 20 mtorr argon with an oxygen partial pressure of 4×10^{-5} torr as measured with an Bayert-Alpert type ionization gauge. Thin films were patterned into MOS capacitors (size range 4×10^{-3}cm^2 to 0.26 cm^2) through contact lithography and liftoff processing. The sputter-deposited CuO layers were measured to be 200 nm thick by profilometry. As prepared Cu_2O and CuO film stoichiometry were characterized by x-ray photoelectron spectroscopy and glancing-incidence x-ray diffraction (GI-XRD)(B. E. McCandless, IEC, University of Delaware)[14].

X-ray photoelectron studies were carried out using a PHI-5600 XPS instrument equipped with an Al K_α X-ray source monochromated to 1486.6 eV. Photoelectron energies were initially calibrated using standard procedures to the Au $4f$ standard value of 84.0 eV. Argon sputtering that was employed removes any adventitious carbon from the surface, so we are unable to use that as an internal reference during the course of the photoemission. The chamber pressure was maintained at approximately 7×10^{-10} torr during the course of the analysis. Concentration depth profiling of the film was achieved using a rastered 3 kV Ar+ ion beam. Five minute sputter intervals were employed and XPS

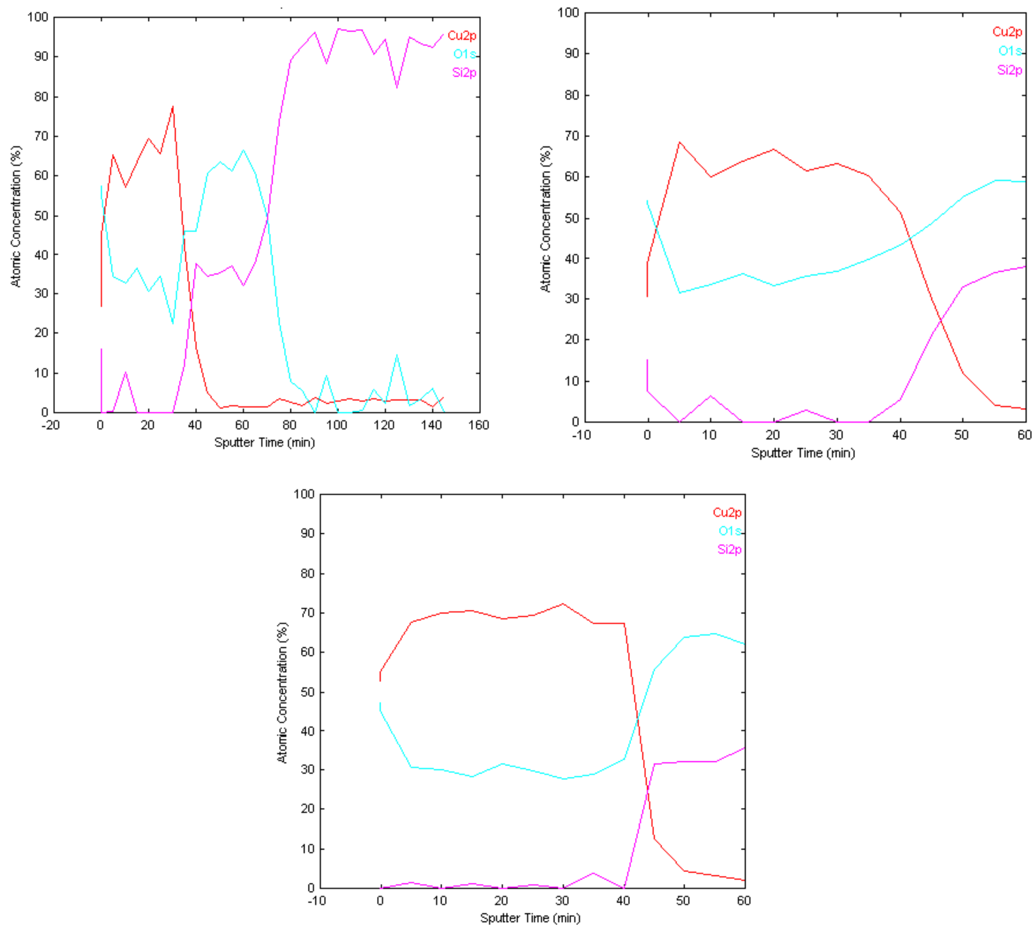

Figure 8.1: Compositional Depth Profile showing variation of Copper, Oxygen and Silicon concentration with depth: (a, b) – thermal oxidation of Cu films; (c) – prepared by reactive sputtering

analysis of the newly exposed surface was done until the silicon substrate was reached.

Electrical measurements were made in the Willis Group in a vacuum probe station and electrical current measurements and applied voltages were measured with an electrometer (Keithley). The applied voltages refer to the voltage applied to the metal electrode. The silicon substrates had a backside coating of aluminum for ohmic contact[14].

8.3 Results & Discussion

Films corresponding to figures 8.2 (a) and (b) were prepared by thermal oxidation of Cu films, while film (c) was prepared by reactive sputtering. Interpretation of GIXRD data (not shown) shows film (a) to contain Cu_2O and CuO phases, while films (b) and (c) contain only CuO. Figure 8.1 shows the variation of composition as a function of depth as obtained with argon sputtering. The sputter rate of the copper oxide is estimated to be around 25-40 Å/minute given that the silicon substrate is reached in about 40 minutes and the thickness of the copper was measured to be around 100-150 nm by profilometry.

Figure 8.2 a-c plots Cu $2p$ photoelectron spectra as a function of the number of sputtering cycles for the thermally oxidized and reactively sputtered Cu_2O and CuO samples. Figure 8.2(a) shows that the sample surface has a Cu binding energy characteristic of CuO and also exhibits the characteristic CuO satellite feature. The lower intensity of the first copper spectrum before sputtering can be attributed to the adventitious hydrocarbons that attenuate the copper signal. The bulk of the Cu $2p^{3/2}$ exhibits a binding energy of 932.5 eV, which could be attributed to either CuO or to Cu_2O (Cu(I) and Cu(0) have very nearly identical Cu $2p^{3/2}$ binding energies). Based on the GIXRD data and the XPS O signal (not shown), the bulk of the film is Cu_2O with a surface CuO layer from ambient exposure. Figure 8.2 (b) corresponds to films oxidized at higher temperatures. The XPS spectra reflect the presence of CuO well into the film and not just at the surface, corroborating the XRD data. The peak energy of the Cu $2p^{3/2}$ is also shifted to 932.8 V and it exhibits the satellite feature of the Cu^{2+} oxide. Figure 8.2(c) is acquired from the sample that was sputter deposited from a CuO target, and it exhibits characteristics of CuO all through the film. The Cu $2p^{3/2}$ binding energy of 932.8 eV, and the satellite is again observed. Due to the possibility of charging and the lack of a good internal standard, the reported binding energies of the peaks acquired during sputtering are not likely to be accurate. However, the presence of the satellite in the $2p^{3/2}$ is a good indicator for

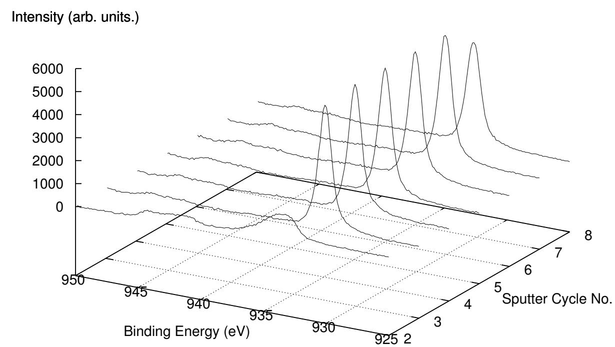

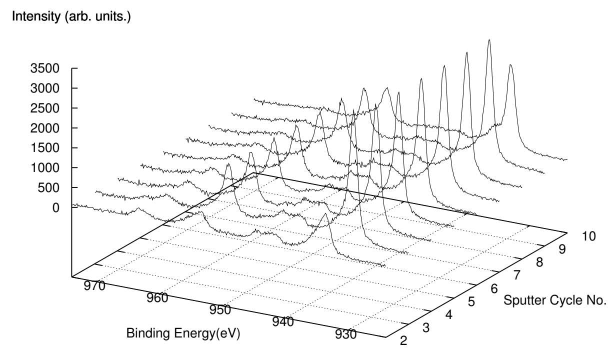

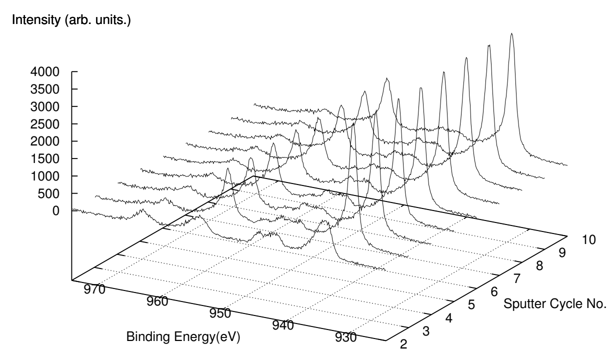

Figure 8.2: Copper 2 *p* Depth Profile: (a, b) – thermal oxidation of Cu films; (c) – prepared by reactive sputtering

the presence of Cu(II). Preferential sputtering of the oxygen atoms is also a problem inherent in the analysis this causes the computed stoichiometry to be relatively copper rich (e.g. in samples apparently CuO the Cu:O composition is 65:35). However, because the photoelectron escape depth is greater than the sputter damage depth, the binding energies of the observed copper peaks allows us to make conclusions regarding the nature of the oxides in the films.

Figure 8.3 shows the O 1*s* evolving with depth. The oxidation state of oxygen is obviously different in the copper as opposed to the silicon. This may be surprising since electronegativity wise, copper and silicon have Pauling electronegativities of approximately 1.9 each. Due the different nature of preparation of the oxide though, the oxygen is bound to be bonded stronger to the silicon than to the copper and hence the shifts in binding energies.

8.4 Conclusions

X-ray photoemission studies of various copper films studied by sputter depth profiling various copper oxide films was able to characterize the oxidative state of the film as a function of depth. This correlated well with glancing-incidence x-ray diffraction data for the film. The composition as a function of depth was determined. This data supported conclusions that the larger study made, regarding the investigation of the oxygen dependence of copper ion transport in SiO_2 dielectrics which demonstrated that the copper ion transport depended on oxygen pressure and oxidation state as well as temperature and applied electrical bias. Copper Ion flux measurements (not shown) of Cu_2O and CuO films showed that the flux is low under vacuum conditions and increases with oxygen pressure until saturation at high oxygen pressure. Since the ion flux was seen to be significantly larger for the CuO films as compared to the Cu_2O films, and sputter deposited CuO films have a higher flux than thermally oxidized CuO films, the data indirectly suggested that Cu^{++} ions may be more mobile at the copper/SiO_2 interface, though further study is needed for direct evidence.

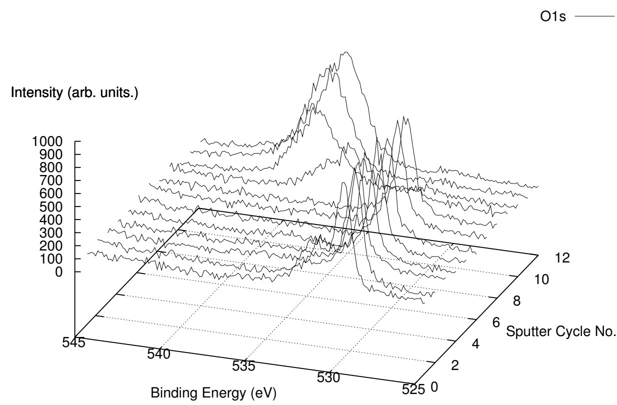

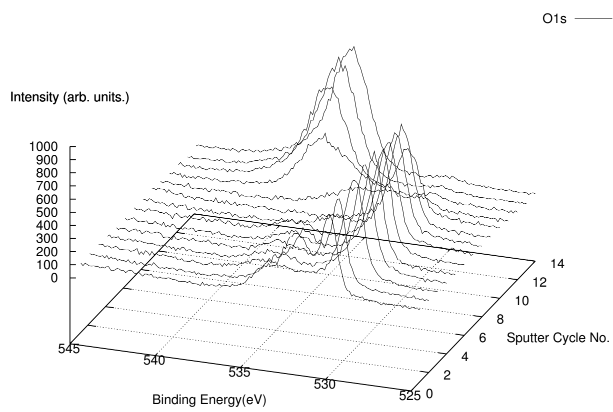

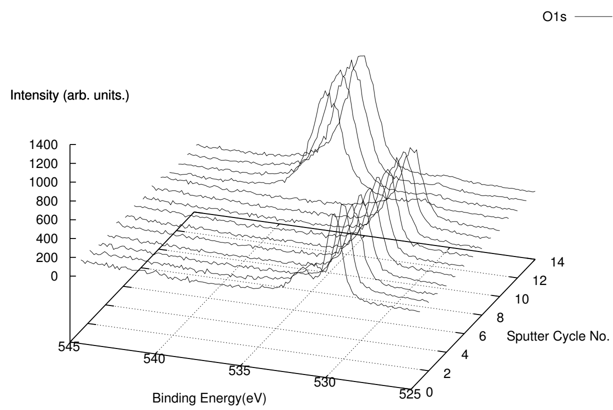

Figure 8.3: Oxygen 1*s* Depth Profile: (a, b) – thermal oxidation of Cu films; (c) – prepared by reactive sputtering

Chapter 9

FUTURE WORK

9.1 Interfacial Charge

The inversion layer mobility of devices incorporating high-κ dielectrics is almost always substantially reduced. This mobility reduction is caused not only by remote phonon scattering[61] and surface roughness effects, but also due to charge accumulation at the interfaces. Previous studies have investigated interfacial charges using Capacitance-Voltage (C-V) measurements[62]. We propose using photoemission to probe these interfaces for the presence of interfacial charge; the presence of positive or negative interfacial charges affects the position of the photoemission peak. Sambe and Ramaker[63] describes the change in photoelectron kinetic energy in the case of a dipole at the Al-Al_2O_3 interface. As shown in the work done by Cazaux[64, 65] and Edgell *et al.*[66], photoemission peaks can also shift due to accumulated charges induced by photoemission, externally introduced or pre existing interfacial charges. Opila *et. al.*[16] have estimated the interfacial charge as

$$\Delta\phi = Qd_2[-\frac{d_1}{\epsilon_1} - \frac{d_2}{2\epsilon_1} - \frac{d_2}{2\epsilon_2}] \tag{9.1}$$

where: $Qd_2 = \frac{charge}{cm^2}$ in the oxide

$\Delta\phi$ = change in potential

ϵ_1, ϵ_2 = relative dielectric constants of substrate, oxide

d_1, d_2 = distance from the interface to end of screening charge region in substrate, oxide.

The current study would attempt to compare films deposited via thermal ALD vs. plasma enhanced ALD and attempt quantification of charge at the interface and correlate

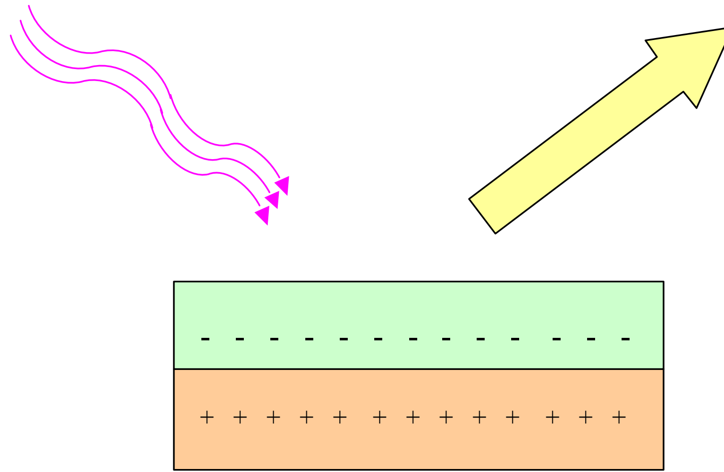

Figure 9.1: Presence of interfacial charges in the system affect the binding energies of the emitted photoelectrons.

it with measurements from other techniques such as C-V measurements. Other interesting comparisons would involve comparing differences between nitrided and non-nitrided samples. Introducing nitrogen into silicon oxide to form the oxynitride has been shown to suppress boron penetration, alleviate interfacial strain, enhance reliability, and improve hot carrier resistance compared to SiO_2[15, 67, 68]. Similar effects in the current system could possibly be correlated to changes in the interfacial charge. The amount of interfacial SiO_2 layer created would be expected to affect the amount of interfacial charge as well. Differences as a function of plasma power employed in case of PEALD are also a possible avenue for investigation. Capacitor measurements and Kelvin probe measurements would be complementary techniques for comparison.

BIBLIOGRAPHY

[1] G.E. Moore. In *International Solid State Circuits Conference (ISSCC)*, 2003.

[2] G.E. Moore. *Electronics*, 38:114, 1965.

[3] G. D. Wilk, R. M. Wallace, and J. M. Anthony. High-kappa gate dielectrics: Current status and materials properties considerations. *Journal of Applied Physics*, 89(10):5243–5275, 2001.

[4] G. Lucovsky and J. Whitten. In M. Houssa, editor, *High-κ dielectrics*, pages 325–326. Institute of Physics Publishing, Bristol, 2004.

[5] M. Leskela and M. Ritala. Atomic layer deposition (ALD): from precursors to thin film structures. *Thin Solid Films*, 409(1):138–146, 2002.

[6] M. Leskela and M. Ritala. Atomic layer deposition chemistry: Recent developments and future challenges. *Angewandte Chemie-International Edition*, 42(45):5548–5554, 2003.

[7] O. Sneh, R. B. Clark-Phelps, A. R. Londergan, J. Winkler, and T. E. Seidel. Thin film atomic layer deposition equipment for semiconductor processing. *Thin Solid Films*, 402(1-2):248–261, 2002.

[8] J. S. Moodera and G. Mathon. Spin polarized tunneling in ferromagnetic junctions. *Journal of Magnetism and Magnetic Materials*, 200(1-3):248–273, 1999.

[9] J. S. Moodera, T. H. Kim, C. Tanaka, and C. H. De Groot. Spin-polarized tunnelling, magnetoresistance and interfacial effects in ferromagnetic junctions. *Philosophical Magazine B-Physics of Condensed Matter Statistical Mechanics Electronic Optical and Magnetic Properties*, 80(2):195–206, 2000.

[10] E. Y. Tsymbal, O. N. Mryasov, and P. R. LeClair. Spin-dependent tunnelling in magnetic tunnel junctions. *Journal of Physics-Condensed Matter*, 15(4):R109–R142, 2003.

[11] S. P. Murarka, I. V. Verner, and R. J. Gutmann. *Copper-Fundamental Mechanisms for Microelectronic Applications*. John Wiley & Sons, Inc., 2000.

[12] A. E. Kaloyeros and E. Eisenbraun. Ultrathin diffusion barriers/liners for gigascale copper metallization. *Annual Review Of Materials Science*, 30:363–385, 2000.

[13] B. G. Willis and D. V. Lang. Oxidation mechanism of ionic transport of copper in SiO_2 dielectrics. *Thin Solid Films*, 467:284–293, 2004.

[14] L.P. Shepherd, A. Mathew, B. E. McCandless, and B. G. Willis. Oxygen pressure dependence of copper ion transport in SiO_2 dielectrics. *Journal of Vacuum Science and Technology,* In Press, 2006.

[15] J. P. Chang, M. L. Green, V. M. Donnelly, R. L. Opila, J. Eng, J. Sapjeta, P. J. Silverman, B. Weir, H. C. Lu, T. Gustafsson, and E. Garfunkel. Profiling nitrogen in ultrathin silicon oxynitrides with angle-resolved X-ray photoelectron spectroscopy. *Journal of Applied Physics*, 87(9):4449–4455, 2000.

[16] R. L. Opila, G. D. Wilk, M. A. Alam, R. B. van Dover, and B. W. Busch. Photoemission study of Zr- and Hf-silicates for use as high-kappa oxides: Role of second nearest neighbors and interface charge. *Applied Physics Letters*, 81(10):1788–1790, 2002.

[17] G. D. Wilk and D. A. Muller. Correlation of annealing effects on local electronic structure and macroscopic electrical properties for HfO_2 deposited by atomic layer deposition. *Applied Physics Letters*, 83:3984–3986, 2003.

[18] M. M. Frank, Y. J. Chabal, and G. D. Wilk. Nucleation and interface formation mechanisms in atomic layer deposition of gate oxides. *Applied Physics Letters*, 82:4758–4760, 2003.

[19] M. Y. Ho, H. Gong, G. D. Wilk, B. W. Busch, M. L. Green, P. M. Voyles, D. A. Muller, M. Bude, W. H. Lin, A. See, M. E. Loomans, S. K. Lahiri, and P. I. Raisanen. Morphology and crystallization kinetics in HfO_2 thin films grown by atomic layer deposition. *Journal Of Applied Physics*, 93:1477–1481, 2003.

[20] G. Lucovsky and J. C. Phillips. Defects and defect relaxation at internal interfaces between high-κ transition metal and rare earth dielectrics and interfacial native oxides in metal oxide semiconductor (MOS) structures. *Thin Solid Films*, 486:200–204, 2005.

[21] G. Lucovsky, G. B. Rayner, D. Kang, C. L. Hinkle, and J. G. Hong. A spectroscopic study distinguishing between chemical phase separation with different degrees of crystallinity in Hf(Zr) silicate alloys. *Applied Surface Science*, 234:429–433, 2004.

[22] G. Lucovsky, J. G. Hong, C. C. Fulton, Y. Zou, R. J. Nemanich, H. Ade, D. G. Scholm, and J. L. Freeouf. Spectroscopic studies of metal high-κ dielectrics: transition metal oxides and silicates, and complex rare earth/transition metal oxides. *Physica Status Solidi B-Basic Research*, 241:2221–2235, 2004.

[23] G. Lucovsky. Electronic structure of transition metal/rare earth alternative high-κ gate dielectrics: interfacial band alignments and intrinsic defects. *Microelectronics Reliability*, 43:1417–1426, 2003.

[24] C. C. Fulton, G. Lucovsky, and R. J. Nemanich. Electronic states at the interface of Ti-Si oxide on Si(100). *Journal Of Vacuum Science & Technology B*, 20:1726–1731, 2002.

[25] H. Y. Yu, N. Wu, M. F. Li, C. X. Zhu, B. J. Cho, D. L. Kwong, C. H. Tung, J. S. Pan, J. W. Chai, W. D. Wang, D. Z. Chi, C. H. Ang, J. Z. Zheng, and S. Ramanathan. Thermal stability of $(HfO_2)_x(Al_2O_3)_{1-x}$ on Si. *Applied Physics Letters*, 81(19):3618–3620, 2002.

[26] H. Y. Yu, M. F. Li, B. J. Cho, C. C. Yeo, M. S. Joo, D. L. Kwong, J. S. Pan, C. H. Ang, J. Z. Zheng, and S. Ramanathan. Energy gap and band alignment for $(HfO_2)_x(Al_2O_3)_{1-x}$ on (100) Si. *Applied Physics Letters*, 81(2):376–378, 2002.

[27] G. M. Rignanese and A. Pasquarello. Nitrogen bonding configurations at nitrided Si(001) surfaces and Si(001)-SiO2 interfaces: A first-principles study of core-level shifts. *Physical Review B*, 6307, 2001.

[28] G. M. Rignanese and A. Pasquarello. First-principles study of NH_3 exposed Si(001)2x1: Relation between N 1*s* core-level shifts and atomic structure. *Applied Physics Letters*, 76:553–555, 2000.

[29] G. M. Rignanese, A. Pasquarello, J. C. Charlier, X. Gonze, and R. Car. Nitrogen incorporation at Si(001)-SiO_2 interfaces: Relation between N 1*s* core-level shifts and microscopic structure. *Physical Review Letters*, 79:5174–5177, 1997.

[30] S. Ramanathan, P. C. McIntyre, J. Luning, P. S. Lysaght, Y. Yang, Z. Q. Chen, and S. Stemmer. Phase separation in hafnium silicates for alternative gate dielectrics - influence on the unoccupied states. *Journal of the Electrochemical Society*, 150(10):F173–F177, 2003.

[31] S. Stemmer, Z. Q. Chen, R. Keding, J. P. Maria, D. Wicaksana, and A. I. Kingon. Stability of ZrO_2 layers on Si (001) during high-temperature anneals under reduced oxygen partial pressures. *Journal of Applied Physics*, 92(1):82–86, 2002.

[32] S. Stemmer, Y. L. Li, B. Foran, P. S. Lysaght, S. K. Streiffer, P. Fuoss, and S. Seifert. Grazing-incidence small angle X-ray scattering studies of phase separation in hafnium silicate films. *Applied Physics Letters*, 83(15):3141–3143, 2003.

[33] S. Stemmer. Thermodynamic considerations in the stability of binary oxides for alternative gate dielectrics in complementary metal-oxide-semiconductors. *Journal of Vacuum Science & Technology B*, 22(2):791–800, 2004.

[34] J. W. Cahn. Phase separation by spinodal decomposition in isotropic systems. *The Journal of Chemical Physics*, 42(1):93–99, 1965.

[35] S. Monaghan, J. C. Greer, and S. D. Elliott. Thermal decomposition mechanisms of hafnium and zirconium silicates at the atomic scale. *Journal of Applied Physics*, 97(11), 2005.

[36] G. B. Rayner, D. Kang, and G. Lucovsky. Chemical phase separation in Zr silicate alloys: a spectroscopic study distinguishing between chemical phase separation with different degrees of micro- and nano-crystallinity. *Journal of Non-Crystalline Solids*, 338-40:151–154, 2004.

[37] S. Sayan, E. Garfunkel, T. Nishimura, W. H. Schulte, T. Gustafsson, and G. D. Wilk. Thermal decomposition behavior of the $HfO_2/SiO_2/Si$ system. *Journal of Applied Physics*, 94(2):928–934, 2003.

[38] P. Lysaght, B. Foran, S. Stemmer, G. Bersuker, J. Bennett, R. Tichy, L. Larson, and H. R. Huff. Thermal response of MOCVD hafnium silicate. *Microelectronic Engineering*, 69(2-4):182–189, 2003.

[39] W. Nieveen. *Unpublished Result*, 2005.

[40] P. J. Cumpson. Angle-resolved XPS and AES - depth-resolution limits and a general comparison of properties of depth-profile reconstruction methods. *Journal of Electron Spectroscopy and Related Phenomena*, 73(1):25–52, 1995.

[41] A. K. Livesey and G. C. Smith. The determination of depth profiles from angle-dependent XPS using maximum-entropy data-analysis. *Journal of Electron Spectroscopy and Related Phenomena*, 67(3):439–461, 1994.

[42] G. C. Smith and A. K. Livesey. Maximum-entropy - a new approach to nondestructive deconvolution of depth profiles from angle-dependent XPS. *Surface and Interface Analysis*, 19(1-12):175–180, 1992.

[43] R. K. Bryan. Maximum-entropy analysis of oversampled data problems. *European Biophysics Journal*, 18(3):165–174, 1990.

[44] E. W. A. Young and V. Kaushik. Device integration issues. In M. Houssa, editor, *High-κ dielectrics*, pages 517–522. Institute of Physics Publishing, Bristol, 2004.

[45] C. Hobbs, L. Fonseca, V. Dhandapani, S. Samavedam, B. Taylor, J. Grant, L. Dip, D. Triyoso, R. Hegde, R. Gilmer, D. Garcia, D. Roan, L. Lovejoy, R. Rai, L. Hebert, B. Tseng, H. White, and P. Tobin. Fermi level pinning at the poly-Si/metal oxide interface. *VLSI Technology, 2003. Digest of Technical Papers*, pages 9– 10, 2003.

[46] http://public.itrs.net/. International technology roadmap for semiconductors, 2003.

[47] R. Meservey and P. M. Tedrow. Spin-polarized electron-tunneling. *Physics Reports-Review Section of Physics Letters*, 238(4):173–243, 1994.

[48] R. Meservey, P. M. Tedrow, and P. Fulde. Magnetic field splitting of quasiparticle states in superconducting aluminum films. *Physical Review Letters*, 25(18):1270–1275, 1970.

[49] P. M. Tedrow and R. Meservey. Spin-dependent tunneling into ferromagnetic nickel. *Physical Review Letters*, 26(4):192–195, 1971.

[50] T. Miyazaki and N. Tezuka. Giant magnetic tunneling effect in Fe/Al_2O_3/Fe junction. *Journal of Magnetism and Magnetic Materials*, 139(3):L231–L234, 1995.

[51] J. S. Moodera, J. Nassar, and G. Mathon. Spin-tunneling in ferromagnetic junctions. *Annual Review of Materials Science*, 29:381–432, 1999.

[52] J. S. Moodera, L. R. Kinder, and J. Nowak. Geometrically enhanced magnetoresistance in ferromagnet-insulator-ferromagnet tunnel junctions. *Journal of Applied Physics*, 81(8):5522–5522, 1997. Part 2B.

[53] J. S. Moodera, L. R. Kinder, T. M. Wong, and R. Meservey. Large magnetoresistance at room-temperature in ferromagnetic thin-film tunnel-junctions. *Physical Review Letters*, 74(16):3273–3276, 1995.

[54] J.M. Slaughter, E.Y. Chen, R. Whig, B.N. Engel, J. Janesky, and S. Tehrani. Magnetic tunnel junction materials for electronic applications. *JOM-e*, 52, 2000.

[55] M. Julliere. Tunneling between ferromagnetic-films. *Physics Letters A*, 54(3):225–226, 1975.

[56] G. Landry, Y. Dong, J. Du, X. Xiang, and J. Q. Xiao. Interfacial capacitance effects in magnetic tunneling junctions. *Applied Physics Letters*, 78:501–503, 2001.

[57] F. Braud, J. Torres, J. Palleau, J. L. Mermet, and M. J. Mouche. Ti-diffusion barrier in Cu-based metallization. *Applied Surface Science*, 91:251–256, 1995.

[58] J. Torres. Advanced copper interconnections for silicon CMOS technologies. *Applied Surface Science*, 91:112–123, 1995.

[59] H. Miyazaki, H. Kojima, and K. Hinode. Passivation effect of silicon nitride against copper diffusion. *Journal Of Applied Physics*, 81:7746–7750, 1997.

[60] F. Braud, J. Torres, J. Palleau, J. L. Mermet, C. Marcadal, and E. Richard. Ultra thin diffusion barriers for Cu interconnections at the gigabit generation and beyond. *Microelectronic Engineering*, 33:293–300, 1997.

[61] M. V. Fischetti, D. A. Neumayer, and E. A. Cartier. Effective electron mobility in Si inversion layers in metal-oxide-semiconductor systems with a high-kappa insulator: The role of remote phonon scattering. *Journal of Applied Physics*, 90(9):4587–4608, 2001.

[62] E. H. Nicollian and J. R. Brews. *MOS (Metal Oxide Semiconductor) physics and technology.* John Wiley & Sons, Inc., 1982.

[63] H. Sambe and D. E. Ramaker. X-ray photoelectron-spectroscopy study on the electrical double-layer at an Al_2O_3-Al interface. *Journal of Vacuum Science & Technology a-Vacuum Surfaces and Films*, 10(5):2991–2995, 1992.

[64] J. Cazaux. Mechanisms of charging in electron spectroscopy. *Journal of Electron Spectroscopy and Related Phenomena*, 105(2-3):155–185, 1999.

[65] J. Cazaux. About the charge compensation of insulating samples in XPS. *Journal of Electron Spectroscopy and Related Phenomena*, 113(1):15–33, 2000.

[66] M. J. Edgell, D. R. Baer, and J. E. Castle. Biased referencing experiments for the XPS analysis of nonconducting materials. *Applied Surface Science*, 26(2):129–149, 1986.

[67] E. P. Gusev, H. C. Lu, T. Gustafsson, E. Garfunkel, M. L. Green, and D. Brasen. The composition of ultrathin silicon oxynitrides thermally grown in nitric oxide. *Journal of Applied Physics*, 82(2):896–898, 1997.

[68] G. Lucovsky. Monolayer incorporation of nitrogen at Si-SiO_2 interfaces: Interface characterization and electrical properties. *Journal of Vacuum Science & Technology A-Vacuum Surfaces and Films*, 16(1):356–364, 1998.